

## THE PHYSICS OF THE ‘HEARTBEAT’ STATE OF GRS 1915+105

JOSEPH NEILSEN<sup>1,2</sup>, RONALD A. REMILLARD<sup>3</sup>, JULIA C. LEE<sup>1,2</sup>

*Draft version October 24, 2018*

### ABSTRACT

We present the first detailed phase-resolved spectral analysis of a joint *Chandra* High Energy Transmission Grating Spectrometer and Rossi X-ray Timing Explorer observation of the  $\rho$  variability class in the microquasar GRS 1915+105. The  $\rho$  cycle displays a high-amplitude, double-peaked flare that recurs roughly every 50 s, and is sometimes referred to as the “heartbeat” oscillation. The spectral and timing properties of the oscillation are consistent with the radiation pressure instability and the evolution of a local Eddington limit in the inner disk. We exploit strong variations in the X-ray continuum, iron emission lines, and the accretion disk wind to probe the accretion geometry over nearly six orders of magnitude in distance from the black hole. At small scales (1–10  $R_g$ ), we detect a burst of bremsstrahlung emission that appears to occur when a portion of the inner accretion disk evaporates due to radiation pressure. Jet activity, as inferred from the appearance of a short X-ray hard state, seems to be limited to times near minimum luminosity, with a duty cycle of  $\sim 10\%$ . On larger scales ( $10^5$ – $10^6 R_g$ ) we use detailed photoionization arguments to track the relationship between the fast X-ray variability and the accretion disk wind. For the first time, we are able to show that changes in the broadband X-ray spectrum produce changes in the structure and density of the accretion disk wind on timescales as short as 5 seconds. These results clearly establish a causal link between the X-ray oscillations and the disk wind and therefore support the existence of a disk-jet-wind connection. Furthermore, our analysis shows that the mass loss rate in the wind may be sufficient to cause long-term oscillations in the accretion rate, leading to state transitions in GRS 1915+105.

*Subject headings:* accretion, accretion disks — black hole physics — instabilities — binaries: close — stars: winds, outflows — X-rays: individual (GRS 1915+105)

### 1. INTRODUCTION

Accreting stellar-mass black holes are known to exhibit different accretion ‘states,’ which are usually defined in terms of their X-ray spectral shape and variability (Remillard & McClintock 2006 and references therein). Physically, these states are intimately related to the fundamental parameters of the accretion flow, e.g. the accretion rate, the accretion disk geometry, the radiative efficiency of the disk, and the role of outflows in the form of winds and jets. The fact that X-ray binaries (XRBs) undergo state transitions highlights the dynamic nature of accretion onto black holes and allows for the possibility of determining not only the fundamental parameters of accretion but also the physics that controls them.

Of all the known Galactic black holes, GRS 1915+105 is undoubtedly the most prolific source of state transitions. Discovered as a transient by GRANAT in 1992 (Castro-Tirado et al.), it has remained in outburst for the last 18 years and is typically one of the very brightest sources in the X-ray sky. It is also one of the most variable: its X-ray lightcurve consists of at least 14 different patterns of variability, most of which are high amplitude and highly-structured (Belloni et al. 2000, hereafter B00; Klein-Wolt et al. 2002; Hannikainen et al. 2005). It is believed that many of these phenomenologically-described variability classes,

which are labeled with Greek letters (B00), are limit cycles of accretion and ejection in an unstable disk (Belloni et al. 1997a; Mirabel et al. 1998; Tagger et al. 2004; Fender & Belloni 2004).

The diverse timing and spectral properties of these variability classes make the behavior of GRS 1915+105 particularly difficult to track in physical detail. Even in the  $\chi$  state, one of the simplest variability classes (with a relatively low X-ray flux, no structured variability, and a hard spectrum), GRS 1915+105 is never as faint or as hard as the canonical ‘hard’ state of black hole binaries (Belloni 2010). On the other hand, the canonical black hole ‘hard’ state is associated with jet production, and GRS 1915+105 has been shown to produce a jet during essentially every spectrally hard interval longer than 100 seconds (Klein-Wolt et al. 2002). This fact suggests that despite some differences in the spectral shape, the physics of jet formation is probably the same for all Galactic black holes (Fender & Belloni 2004).

It is well-established that the properties of jets are highly correlated with the accretion state. But there is now a growing body of evidence suggesting that hot accretion disk winds are equally influenced by the accretion state, in part but not completely due to changes in ionizing flux (Lee et al. 2002; Miller et al. 2006b, 2008; Neilsen & Lee 2009, hereafter Paper I, Ueda et al. 2010; Blum et al. 2010). In Paper I, we demonstrated that the strength of the accretion disk wind in GRS 1915+105 is anticorrelated with the *fractional* hard X-ray flux, which is therefore a useful diagnostic of both the accretion state and outflow physics (for a preliminary discussion of these lines, see Miller et al. 2008). The anticorrelation holds

<sup>1</sup> Astronomy Department, Harvard University, Cambridge, MA 02138; jneilsen@cfa.harvard.edu

<sup>2</sup> Harvard-Smithsonian Center for Astrophysics, Cambridge, MA 02138

<sup>3</sup> MIT Kavli Institute for Astrophysics and Space Research, Cambridge, MA 02139

over many variability classes and there are indications that it may hold for other black holes as well (XTE J1650-500 & GX 339-4, Miller et al. 2004; GRO J1655-40, Miller et al. 2008; H1743-322, Miller et al. 2006b; Blum et al. 2010).

If outflows from stellar-mass black holes depend on the accretion state, then any rapid variability should have observable consequences for those outflows. This is particularly true for GRS 1915+105, where the X-ray spectrum and the accretion flow can change drastically in seconds. For example, it has been shown conclusively that 30-minute radio oscillations are ‘baby jets’ produced by ejection events in cycles like the  $\beta$  state (Fender et al. 1997; Pooley & Fender 1997; Eikenberry et al. 1998; Mirabel et al. 1998; Mirabel & Rodríguez 1999). Accretion disk winds have been directly observed to vary on similar (2–10 ks) timescales (GRS 1915+105: Lee et al. 2002; Ueda, Yamaoka, & Remillard 2009; Ueda et al. 2010; Cir X-1: Schulz & Brandt 2002) or longer (1A 0535+262: Reynolds & Miller 2010). Flux-dependent studies have implied faster variations in both emission (1 s; Miller & Homan 2005) and absorption lines (300 s; Miller et al. 2006b). However, the physical consequences of rapid variability on these winds have yet to be tracked in detail. A potential link between X-ray variability and disk winds would be especially interesting given our recent demonstration of a wind-jet interaction in GRS 1915+105 (Paper I).

In order to explore the relationship between jets, winds, and fast variations in the accretion disk, we have undertaken a detailed investigation of the  $\rho$  variability class in GRS 1915+105. Known affectionately as the ‘heartbeat’ state because of the resemblance of its X-ray lightcurve to an electrocardiogram, the  $\rho$  state (see Fig. 1) is a  $\sim 50$ -s oscillation consisting of a slow rise followed by a series of short bright bursts with amplitudes of order  $5 \times 10^{38}$  ergs  $s^{-1}$  and strong changes in the X-ray spectral hardness (Taam, Chen, & Swank 1997, hereafter TCS97; Vilhu & Nevalainen 1998; Paul et al. 1998). Theoretical models suggest that this state is a manifestation of the Lightman-Eardley instability, a limit cycle in the radiation-pressure dominated inner accretion disk (Lightman & Eardley 1974; Belloni et al. 1997a; Janiuk, Czerny, & Siemiginowska 2000; Nayakshin, Rappaport, & Melia 2000; Janiuk & Czerny 2005).

Previously, we analyzed the average spectrum of a joint *RXTE/Chandra* observation of GRS 1915+105 in the  $\rho$  state (Paper I). We found the average *RXTE* continuum during this observation to be relatively soft, with  $\sim 79\%$  of the 3–18 keV X-ray luminosity ( $L_X \sim 4.9 \times 10^{38}$  ergs  $s^{-1}$ ) emitted below 8.6 keV. In the time-averaged high-resolution X-ray spectrum from the *Chandra* High-Energy Transmission Grating Spectrometer (HETGS; Canizares et al. 2005), we detected an Fe XXVI Ly $\alpha$  absorption line from the accretion disk wind with an equivalent width of  $-7.2 \pm 1.7$  eV and a blueshift of  $\sim 1400$  km  $s^{-1}$ .

We follow up in this paper by tracking the  $\rho$ -phase-resolve timing and spectral variability of this same joint *RXTE/Chandra* HETGS observation of GRS 1915+105. For the very first time, we detect significant variations in absorption lines in phase-binned spectra, allowing us to

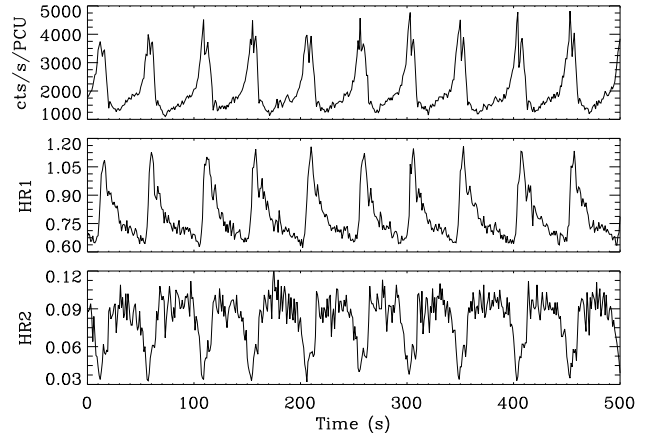


FIG. 1.— The 1-second PCA heartbeat lightcurve (top panel), HR1 (middle panel), and HR2 (bottom panel).  $HR1 \equiv B/A$  and  $HR2 \equiv C/B$ , where  $A$ ,  $B$ , and  $C$  are the PCA count rates in the 2.0–4.5 keV, 4.5–9.0 keV, and 9.0–30 keV bands. The heartbeat is composed of a slow rise or a shoulder followed by a double-peaked pulse. In HR1 the behavior is similar, although the shoulder follows the maximum rather than preceding it.

assess real physical changes on timescales of seconds, well below the dynamical time in the wind. We explain the origin and evolution of the accretion disk wind via analysis of the X-ray spectral variability. Our results indicate that each bright burst has a significant impact on the accretion dynamics from the innermost to the outermost regions of the accretion disk.

In Section 2 we describe our observations and data reduction. In Section 3, we define the phase of the  $\rho$  cycle, explore variations in the recurrence time, and analyze phase-resolved power spectra. We perform joint spectral analysis with *RXTE* and the *Chandra* HETGS in Section 4. We discuss our results on outflow formation and disk instabilities in Section 5, summarize our understanding of the oscillation in Section 6, and conclude in Section 7.

## 2. OBSERVATIONS AND DATA REDUCTION

### 2.1. *Chandra* Data

GRS 1915+105 was observed with the *Chandra* HETGS on 2001 May 23 (08:25:38 UT), for 30.16 ks. In order to mitigate pileup, the data were taken in Continuous Clocking Mode; events were recorded in Graded format to reduce the risk of telemetry saturation.

We reduced and barycenter-corrected the *Chandra* data using standard tools from the CIAO analysis suite, version 4.0. After reprocessing and filtering, we extracted High-Energy Grating (HEG) spectra and created grating responses. We used the order-sorting routine to remove the ACIS S4 readout streak, since the *destreak* tool can introduce spectral artifacts for bright continuum sources like GRS 1915+105. We extracted 1-second lightcurves with *dmextract*.

Due to incomplete calibration of Charge-Transfer Inefficiency (CTI) in CC/Graded mode, there is some wavelength-dependent disagreement in the continuum flux between spectral orders of the HEG (and the MEG, which we do not consider here because of its lower spectral resolution). For this reason, it is not currently possible to fit a physical continuum model to the HETGS data. Instead, we fit the individual spectra

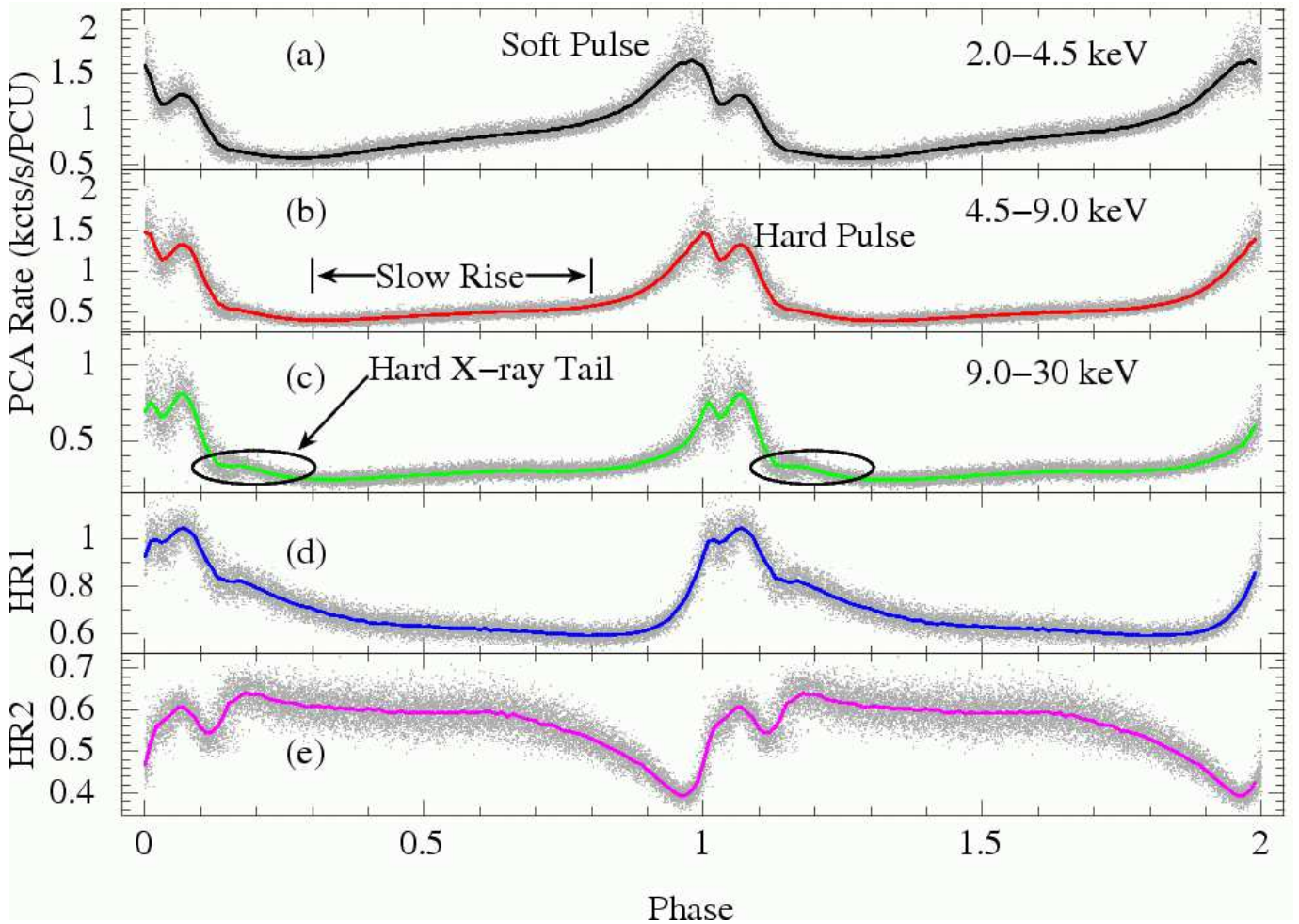


FIG. 2.— The phase-folded PCA heartbeat lightcurve in the (a)  $A \equiv 2\text{--}4.5$  keV, (b)  $B \equiv 4.5\text{--}9.0$  keV, and (c)  $C \equiv 9.0\text{--}30$  keV bands, along with (d) HR1 and (e) HR2, which are defined in Section 3. As discussed in the text, the mean period is about 50 seconds, so each major tick represents about 5 seconds. We have labeled the slow rise ( $\sim 25$  s), the soft and hard pulses, and the hard X-ray tail ( $\sim 5\text{--}10$  s). Two cycles are shown for clarity. The gray points in the background are the individual data points, showing remarkable consistency despite noticeable variations in the cycle period.

with polynomials to model the local continuum and use Gaussians for line features found in the combined residuals.

### 2.2. *RXTE* Data

During the *Chandra* observation, *RXTE* made a pointed observation of GRS 1915+105, beginning on 2001 May 23 at 11:08:20.8 UT and lasting 21.9 ks (elapsed) with 13.7 ks exposure time. We select all available data subject to the following constraints: (1) the Earth-limb elevation angle is above  $3^\circ$ ; (2) the spacecraft is outside the South Atlantic Anomaly; (3) the offset angle from GRS 1915+105 is less than  $0.02^\circ$ . In this paper, we analyze the data from the Proportional Counter Array (PCA), which covers the 2–60 keV band.

For timing analysis, we make use of the data from the binned mode B\_8ms\_16A\_0.35\_H\_4P, which covers the 2.0–14.8 keV band at 7.8 ms time resolution, and the event mode E\_16us\_16B\_36\_1s, which covers the 14.8–60 keV band at  $15.3 \mu\text{s}$  time resolution. We extract 1-second barycentered, dead-time-corrected, and background subtracted lightcurves from each of these modes for timing analysis, and use our own software to cre-

ate power spectra, subtracting the dead-time-corrected Poisson noise level after Morgan, Remillard, & Greiner (1997, hereafter MRG97). For high-S/N hardness ratios, we use the energy bands 2–4.5 keV, 4.5–9.0 keV, and 9.0–30 keV, which have roughly equal count rates.

For spectral analysis, the strong fast variability of the  $\rho$  state precludes use of the Standard-2 129-channel spectra, since the 16-second time resolution of the Standard-2 data is too coarse for the 50-second cycles. To compensate, we use the binned mode and event mode data to create 32-channel spectra at 1-s time resolution (see, e.g. TCS97, Belloni et al. 1997a). We treat intervals with different combinations of PCUs separately. Our observation features the PCUs operating in combinations  $\{0, 2, 3, 4\}$  and  $\{1, 2, 3, 4\}$ , with roughly equal exposure times.

### 3. TIMING ANALYSIS

We show a representative portion of the PCA 1-second lightcurve in Figure 1, along with PCA hardness ratios HR1 and HR2 (here defined as the ratio  $B/A$  and  $C/B$ , where A, B, and C are the count rates in the 2.0–4.5 keV, 4.5–9 keV, and 9–30 keV bands, respectively). The lightcurve consists of a  $\sim 25$  second slow rise, followed by a short burst, which is typically double-peaked (see

also Figure 2). HR1 looks rather like the mirror image of the count rate (i.e. flipped horizontally about its maximum), except that HR1 is typically single-peaked. Other instances of the  $\rho$  state have shown different behavior, as the number and relative strengths of the peaks can vary (Massaro et al. 2010, Neilsen et al. 2011, in preparation).

It is our main goal in this section to characterize the timing properties of the  $\rho$  state by tracking the arrival times of each individual burst. We define a phase ephemeris for the oscillation with  $\phi \equiv 0$  at the time of maximum count rate (see the Appendix for the motivation for this choice and the details of our method). This timing analysis is the foundation of all of the results presented in this paper, as it allows us to study the evolution of the X-ray lightcurve, power spectrum, broadband X-ray spectrum, and the high-resolution X-ray spectrum as a function of phase (instead of time).

### 3.1. Phase Ephemeris and Folded Lightcurve

MRG97 tracked individual QPO waves in GRS 1915+105 by fitting functional templates (e.g. sinusoids or Gaussians) to the PCA lightcurve. Given the high amplitude and unusual shape of the lightcurve described here, we opt for a modified version of the MRG97 technique (see the Appendix for more details).

First, we take a single representative cycle from the data and cross-correlate it with the entire lightcurve. Maxima in the normalized cross-correlation values then indicate the times when  $\phi = 0$  (peaks in the count rate). We then fold the data on this first set of  $\phi = 0$  times to obtain the average folded lightcurve. The process is iterated, with the folded lightcurve serving as a new template, to obtain the final set of  $\phi = 0$  times. This analysis results in 623 peak times from the *Chandra* lightcurve and 273 peak times from the PCA lightcurve, which should be accurate to 0.1 seconds or better for *RXTE* and 0.3 seconds or better for *Chandra*. The *RXTE* uncertainty is estimated from the variations produced by the use of different cross-correlation templates, while the *Chandra* uncertainty is derived from the offsets in  $\phi = 0$  times for cycles co-measured with *RXTE* (see the Appendix for details).

We also explored the 3-D pathway of the  $\rho$  cycle through the hardness-hardness-intensity diagram (HHID; see Soleri et al. 2008 for an example of this method) to consider using the mean pathway to construct a set of phase-resolved spectra that could be analyzed and compared to the results derived from the cross-correlation ephemeris method. We find that the HHID method is less suitable for the  $\rho$  cycle because the statistical noise for 1 s bins causes significant scatter in the HHID (particularly in the hard color dimension), and because the rho cycle shows a tight loop in all three parameters over the phase interval 0.04-0.12, causing some degeneracy for phase tracking based on the HHID. Thus we believe cross-correlations provide the optimal characterization of the cyclic variability. With a phase ephemeris defined, we can create phase-folded lightcurves and hardness ratios (Figure 2). It is clear from this figure that phase-folding is a very effective way to characterize the oscillation, since the individual cycles have very similar shapes: the cycle-to-cycle variability is always less than 20% for a given phase.

To help diagnose whether there is systematic noise in-

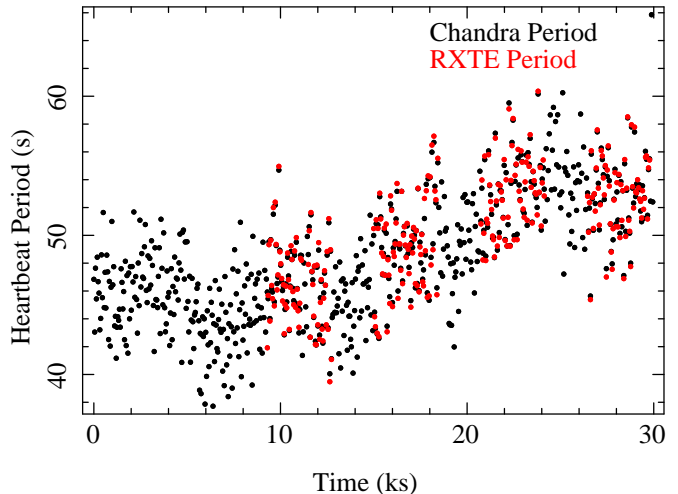


FIG. 3.— The heartbeat period during our observations, measured as the time difference between successive cycles. The periods measured by *Chandra* (black) and *RXTE* (red) show very good agreement. Interestingly, the period exhibits considerable variability on short timescales and drifts slowly over long timescales.

duced by using the broadband count rate to track the heartbeat cycles, compared to a parameter related to spectral shape, we conducted the following test. We used the PCA soft color, i.e. the ratio of source counts at 6-12 keV versus 2-6 keV, as an alternative quantity to compute cross correlations to define the times when each heartbeat cycle begins. The procedures were otherwise left intact. We note that the soft color usually shows one maximum per cycle, which is offset from the times of maximum count rate. The comparison of 239 cycle start times derived from these two tracking parameters (*RXTE* data; mean cycle period 50.488 s) yields an average offset of 3.274 s, with a sample standard deviation of 0.283 s. It is the latter quantity that measures systematic noise differences between the method that uses the count rate to track cycles, versus soft X-ray color. We conclude that neither our phase-resolved lightcurves and binned spectra nor our analysis conclusions would be significantly changed if the heartbeat phases were defined by soft color, since the phase deviations (0.0056) are much less than the spectral bin size (0.02).

During our observation, each folded heartbeat is a slow rise ( $\phi = 0.3 - 0.8 \approx 25$  s), followed by a double-peaked pulse ( $\phi = 0.8 - 0.1 \approx 15$  s) and a hard X-ray tail lasting 5–10 seconds (see  $\phi \sim 0.2$  in panel c). Generally speaking, the slow rise is spectrally hard, the first pulse is soft, and the second pulse is moderately hard, but it is obvious even from Figure 2 that such statements must be made and interpreted only loosely, since HR1 and HR2 are more or less anticorrelated.

Other authors (Janiuk & Czerny 2005; Massaro et al. 2010) have already demonstrated that there is typically a delay between the soft and hard X-ray pulses, as well as a strong relationship between the times between these two bursts and the cycle period. Because HR1 peaks at the hard pulse, we see that the hard X-ray pulse lags the soft X-ray pulse by an average of 3.3 seconds in our observation. This lag increases with the length of the cycle and appears to be a constant 6.5% of the cycle duration. This surprising result implies that the delay between soft

and hard X-ray pulses scales with the same clock as the entire oscillation. It also implies that using an X-ray color to define  $\phi \equiv 0$  simply introduces a phase shift into our results. Note that the variations in the lag are not large enough to interfere with our cross-correlation or phase-folding. We will return to the delay in Sections 4.1 and 5.1.3, where we analyze the X-ray continuum.

### 3.2. The Cycle Period

We define the cycle period as a discrete quantity given by the time difference between two successive times of  $\phi = 0$  in the lightcurve. We show the heartbeat period for *Chandra* and *RXTE* in Figure 3 (black and red, respectively). Two points are immediately clear from this figure, both of which imply that the oscillation period in the  $\rho$  state is similar to that of low-frequency QPOs observed in GRS 1915+105:

1. The heartbeat cycle period exhibits a slow secular drift from  $\sim 45$  seconds to  $\sim 53$  seconds over 30 ks.
2. There is a substantial amount of scatter with an amplitude much higher than the secular drift. This scatter is also much larger than the uncertainty in the cycle period, which is of order 0.1 seconds for *RXTE* measurements (see Section 3.1).

The scatter in the period exemplifies the quasi-periodic nature of the heartbeat cycle: consecutive periods may vary by 5–10 seconds or more. The variability in Figure 3 is reminiscent of the behavior of QPOs in a variety of X-ray states of GRS 1915+105 as seen by MRG97, who tracked the arrival times of individual oscillations for several QPOs with frequencies from 0.067 Hz to 1.8 Hz.

MGR97 were able to demonstrate that the arrival times of these QPOs were well-described by uncorrelated Gaussian noise. For the  $\rho$  state, we find essentially no correlation between successive periods (the autocorrelation coefficient is  $r = -0.018$ ), and the cumulative distribution of periods is fit well with a two-Gaussian model. These Gaussians have mean periods  $\mu_1 = 46.0$  s and  $\mu_2 = 52.8$  s, with standard deviations  $\sigma_1 = 2.2$  s and  $\sigma_2 = 2.1$  s.

The fractional scatter in the period measured here is comparable to the  $\mu = 14.93$  s and  $\sigma = 0.72$  s found by MRG97 for the 0.067 Hz QPO, and is actually less than the scatter measured for the other QPOs they tracked. On the other hand, the drift in the  $\rho$  period is much larger (roughly 40 phase units per 1000 cycles compared to 13 phase units per 1000 cycles for the 0.65 Hz QPO). Given its strong spectral variations, the  $\rho$  cycle is much more complex than a normal QPO, but the variability in its period is quantitatively similar. Given this similarity, it is interesting that a QPO at 6–15 Hz is present in the power spectrum during much of the  $\rho$  state, which is the subject of Section 3.3.

### 3.3. Power Spectra

The phase-folded HR2 curve (Fig. 2) shows two maxima that indicate enhanced hard X-ray components during the hard pulse ( $\phi = 0.05$ – $0.1$ ) and the hard X-ray tail (beginning near  $\phi = 0.15$ ). To help diagnose the spectral conditions during these intervals, we compute power

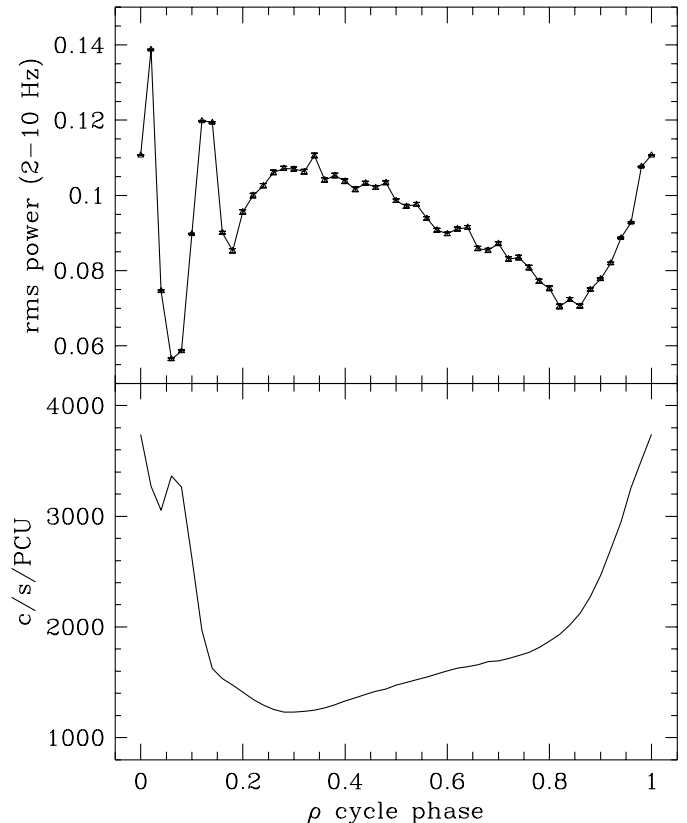


FIG. 4.— 2–10 Hz *rms* power as a function of cycle phase during the  $\rho$  state. We find  $rms > 0.1$  (one of the criteria for the jet-producing X-ray hard state) in three phase windows:  $\phi = 0.02$ ,  $\phi = 0.12$ – $0.14$ , and in a broad interval near  $\phi = 0.3$ . While none of these windows corresponds to the hard pulse in the X-ray lightcurve, the broad interval does overlap with the hard X-ray tail. Thus the later stages of the hard X-ray tail may correspond to a short hard state.

density spectra (PDS) for each second of source exposure with the RXTE PCA, using the count rate in the 2–37.9 keV band. In addition to subtracting the deadtime-corrected Poisson noise (see Section 2.2), we normalize the PDS to units of  $(rms/mean)^2 \text{ Hz}^{-1}$  (MRG97).

To search for possible contributions from a jet during the heartbeat cycle, we hope to exploit the body of evidence that associates a steady radio jet with the properties of the X-ray hard state. The hard state has the signatures of enhanced power ( $rms > 0.1$ ) and a power continuum with “band-limited” shape, i.e., power density that appears flat at frequencies below a few Hz (Muno et al. 2001; Fender 2006; Remillard & McClintock 2006). We note that measurements of *rms* in the literature often integrate the power over the range 0.1–10 Hz, but in this study a lower limit of 2 Hz is dictated by the Nyquist frequency for data samples taken at every second.

We first examine the phase-folded values of *rms* power. This is derived by integrating each PDS over the range 2–10 Hz, and then averaging the results in each of 50 phase bins, using the heartbeat cycle phase ephemeris described in Section 3.1. The phase-folded *rms* curve is shown in Fig. 4. Here we see three maxima that exceed values of 0.1. These occur in narrow phase windows at 0.02 and 0.12–0.14, and in a broad interval near  $\phi = 0.3$ . The first two maxima are likely associated with the intrinsic variability of the oscillation, particularly the sharp



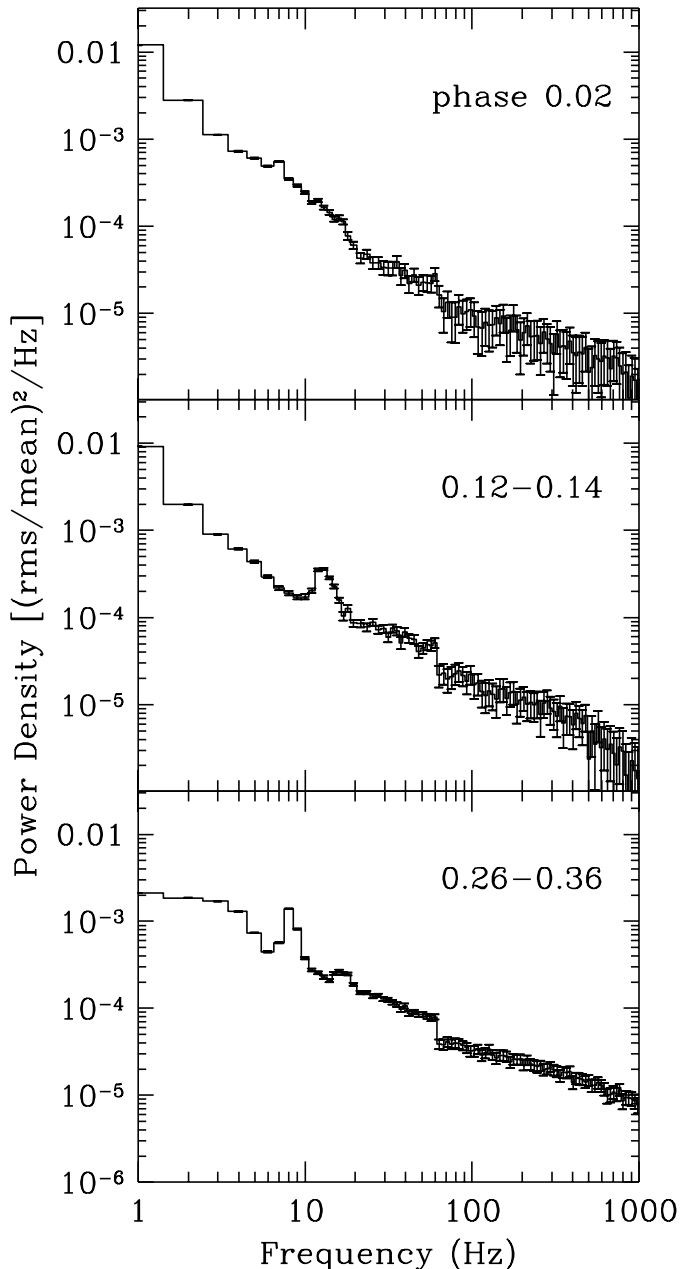


FIG. 5.— Power density spectra (PDS) corresponding to the three *rms* maxima in Figure 4: from top to bottom,  $\phi = 0.02$ ,  $\phi = 0.12-0.14$ , and  $\phi \sim 0.26-0.36$ . During the first and second maxima, the PDS has a power-law shape. It is essentially featureless in the first maximum, but a QPO appears at 13 Hz in the second maximum. The third maximum shows band-limited noise that is consistent with the hard state, along with a QPO at  $\sim 8$  Hz.

decay of the soft and hard pulses, but we cannot rule out contributions from other sources of normal variability. However, none of the three intervals coincides with the hard pulse itself, which is instead aligned with a dip (to  $rms < 0.06$ ) in Fig. 4. On the other hand, there is overlap between the later portions of the hard tail and the broad interval of enhanced *rms* after  $\phi = 0.25$ .

The PDS during the phases corresponding with the three *rms* maxima are shown in Fig. 5. Although the intrinsic variability of the  $\rho$  cycle may artificially enhance the *rms* variability during the first two intervals and could bias the overall slope of the PDS, it is very un-

likely to affect the qualitative shape of power continuum. At phase 0.02, the power density spectrum is featureless and the power density ( $P_\nu$ ) declines with frequency ( $\nu$ ) at a rate slightly steeper than  $P_\nu \propto \nu^{-1}$ . This PDS does not resemble the X-ray hard state. At the time of the second *rms* spike (phase 0.12-0.14), the power continuum again appears with a power-law shape, but there is additionally a QPO near 13 Hz. Finally, the PDS during the third phase interval with enhanced *rms* power does show a band-limited shape that resembles the hard state. Looking at the individual phase-binned PDSs, we find that similar shapes in the power continuum occur during the phase range 0.20-0.36, indicating the most likely interval for contributions from a jet that may temporarily form during each heartbeat cycle.

The low-frequency QPO is detected during phase intervals 0.12-0.82 and 0.96-0.00, and it is therefore much more prevalent than either an elevated *rms* or a power continuum shape that resembles the hard state. The QPO frequency is 14 Hz at  $\phi = 0.12$ , after which it slowly decreases to 7.3 Hz near  $\phi = 0.52$ , and ends near 8 Hz at  $\phi = 0.82$ . As suggested by the bottom panel of Figure 5, a first harmonic is usually present. The presence of a QPO while the source evolves through a long, hard dip in the X-ray lightcurve is reminiscent of the  $\beta$  cycle in GRS 1915+105, which is a 30-min cycle tied to the formation of impulsive radio jets (Markwardt, Swank, & Taam 1999; Mikles, Eikenberry, & Rothstein 2006; Mirabel et al. 1998; Fender & Belloni 2004). Given that the X-ray spectra during the  $\beta$  cycle were successfully interpreted as the combination of thermal radiation from an accretion disk plus a hard X-ray power law attributed to inverse Compton emission, the QPO behavior in the long hard dip of the  $\rho$  cycle may justify application of the inverse Compton model to this state.

However, this leaves behind two puzzles. First, the hard pulse coincides with a phase interval that exhibits neither high *rms* values nor a low-frequency X-ray QPO, and so we find no temporal signatures that might promote spectral interpretation of this hard X-ray component via Comptonization. Secondly, there is another brief appearance of a QPO at phases 0.96-0.00 (with frequency that shifts from 6 to 7 Hz). This QPO is weaker than the 7–14 Hz feature and lacks a first harmonic, so it is difficult to link this short interval to the longer QPO episode. Soleri, Belloni, & Casella (2008) also detected transient QPOs in GRS 1915+105, associating them with state transitions. But because our transient QPO does not coincide with an obvious state transition, the relation between these features is unclear.

Finally, in some phase intervals (0.02–0.06, 0.46–0.50, and 0.68–0.74) there is also weak evidence ( $2.8-3.1\sigma$ ) of a QPO (*rms*  $\sim 1\%$ ) near 60 Hz. This is of interest because GRS 1915+105 is known to exhibit a 67 Hz QPO (MRG97) that can be particularly strong in  $\gamma$ -type lightcurves. A hint of this feature is seen at 59 Hz in the top panel of Fig. 5. At other phases the feature looks more like an edge, as suggested by the bottom panel of Fig. 5. Examination of the PDS in individual phase bins suggests that this edge is *not* an artifact of a stronger QPO moving to lower frequency. These features are too weak to support further analysis, and so this topic is left

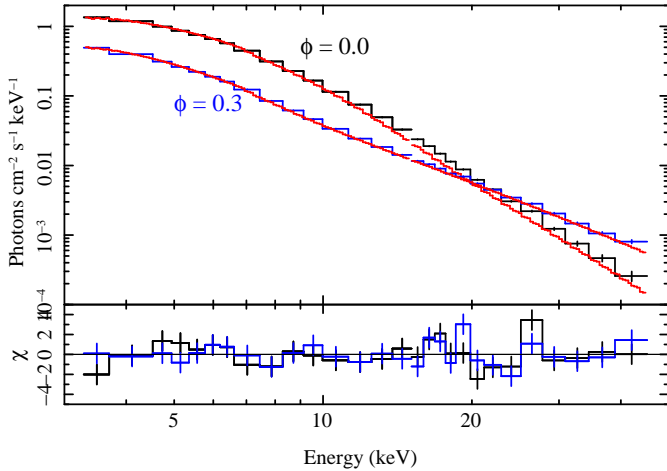


FIG. 6.— PCA spectra and residuals for two different phases of the heartbeat cycle. The fainter spectrum from the cycle minimum (phase  $\phi = 0.3$ ) is significantly flatter than the brighter spectrum at the peak,  $\phi = 0$ . See Section 4.1 for details of our continuum models.

#### 4. SPECTRAL VARIABILITY ANALYSIS

In the following subsections, we explore in detail the spectral variability of the  $\rho$  state, using *RXTE* to study the broadband X-ray properties of the oscillation and the *Chandra* HETGS to probe the known accretion disk wind as a function of  $\rho$  cycle phase. In the previous section, we demonstrated fast spectral evolution in the  $\rho$  state (see also TCS97; B00), but it remains to be seen if and how accretion disk winds and jets participate in this variability. Here we will show that the changes in the X-ray continuum are related to significant variations in the accretion disk wind, both occurring on timescales  $\lesssim 5$  seconds. This constitutes the very first probe of disk wind physics on such short timescales. All spectral fitting is done in ISIS (Houck & Denicola 2000; Houck 2002). We assume a distance and inclination of  $D = 11.2$  kpc and  $i = 66^\circ$  (Fender et al. 1999); we fix  $N_{\text{H}} = 5 \times 10^{22}$   $\text{cm}^{-2}$  (Lee et al. 2002 and references therein).

##### 4.1. *RXTE* PCA

For our variability analysis, we apply our derived phase ephemeris from Section 3.1 to extract phase-resolved spectra: for each 1-second PCA spectrum, we compute the  $\rho$  cycle phase and average the results using 50 phase bins. At each phase, we fit the spectrum from 3.3 to 45 keV. X-ray spectra of black hole binaries have been modeled as the combination of various soft and hard components, which may include but are not limited to: thermal radiation from the accretion disk, power law emission, an explicit treatment of Comptonization, or bremsstrahlung emission. For the highly variable states of GRS 1915+105, a model consisting of a multi-temperature accretion disk plus some type of power law has been especially effective at tracking the relative changes in the accretion disk and Comptonization (see e.g. Belloni et al. 1997a; Migliari & Belloni 2003).

We focus here on the variations of the accretion disk and hard X-ray components inferred from several different continuum models. We show two example phase-resolved PCA spectra (from the peak and minimum of

the oscillation) in Figure 6. As expected from our energy-resolved lightcurves, the spectrum at the peak of the count rate ( $\phi = 0$ ) is significantly brighter and softer than the flat spectrum at the cycle minimum ( $\phi = 0.3$ ).

##### 4.1.1. Model 1: *simpl*

Our initial model for the X-ray continuum consists of five components: cold absorption (*tbabs*; Wilms, Allen, & McCray 2000), a hot disk component (*ezdiskbb*; Zimmerman et al. 2005), an emission line at 6.4 keV (*egauss*), a high-energy cutoff (*highcut*, whose formula is given by  $\exp(E/E_{\text{fold}})$ ), plus a scattering component (*simpl*; Steiner et al. 2009). *simpl* is a convolution model that takes any seed spectrum and scatters a fraction  $f_{\text{SC}}$  of the photons into a power law. The high-energy cutoff is required to account for curvature in the hard X-ray spectrum, and we choose *simpl* because it conserves photons and avoids the divergence of the *powerlaw* model from realistic expectations of Comptonization at low energies. We allow the different PCU combinations to have different parameters, although we tie the high-energy cutoff parameters together for better constraints. In the end, our best fit parameters for the different PCU sets typically differ by  $\lesssim 1\sigma$ . Model 1 provides an excellent statistical description of the X-ray continuum at nearly all phases of the  $\rho$  cycle (overall  $\chi^2/\nu = 2301.9/2150 = 1.07$ ), but the parameters during the hard pulse ( $\phi \sim 0.06$ ) are somewhat puzzling. See below and Section 4.1.3 for more details and alternative explanations.

We show the results of our broadband spectral fits in Figure 7. In these fits, the observed maximum temperature in the disk  $T_{\text{obs}}$  hovers around 1.1–1.2 keV for the majority of the cycle, spiking sharply to  $\sim 2.2$  keV during the X-ray burst. At the same time, the inner radius of the disk is relatively large (70–110 km) and grows during the slow rise, dropping swiftly to  $\sim 40$  km at the end of the soft pulse. The inner radius  $R_{\text{in}}$  is related to the *ezdiskbb* normalization  $N_{\text{disk}}$  as (Zimmerman et al. 2005):

$$N_{\text{disk}} = \frac{1}{f^4} \left( \frac{R_{\text{in}}}{D} \right)^2 \cos i. \quad (1)$$

Because *simpl* counts photons when calculating the disk normalization and the power law ( $f_{\text{SC}}$ ),  $N_{\text{disk}}$  in Model 1 uniquely tracks the disk parameters *prior* to Comptonization. For the high luminosities here, we use a color correction factor  $f = 1.9$  (J. Steiner, private communication). The results are qualitatively similar to the fast variations seen by Belloni et al. (1997b,a) in the  $\kappa$  and  $\lambda$  states, although their disk radii are a factor of  $\sim 2$  lower than ours. This difference appears to be mainly due to our use of *ezdiskbb* rather than *diskbb*. Thus it does not indicate a physical difference between the  $\rho$  state and the  $\kappa$  and  $\lambda$  states.

During the slow rise the photon index  $\Gamma$  is stable around 2.1, which is relatively steep for a hard state but not unusual for GRS 1915+105. But near  $\phi = 0$ , the  $\Gamma$  displays a double-peaked phase dependence, rising quickly to its upper limit ( $\Gamma = 4$ ; Steiner et al. 2009), dropping sharply back to  $\sim 2.5$  during the hard pulse, then peaking again near 4. After the pulses,  $\Gamma$  decays exponentially back to 2 with an  $e$ -folding interval  $\Delta\phi \sim 0.1$ .

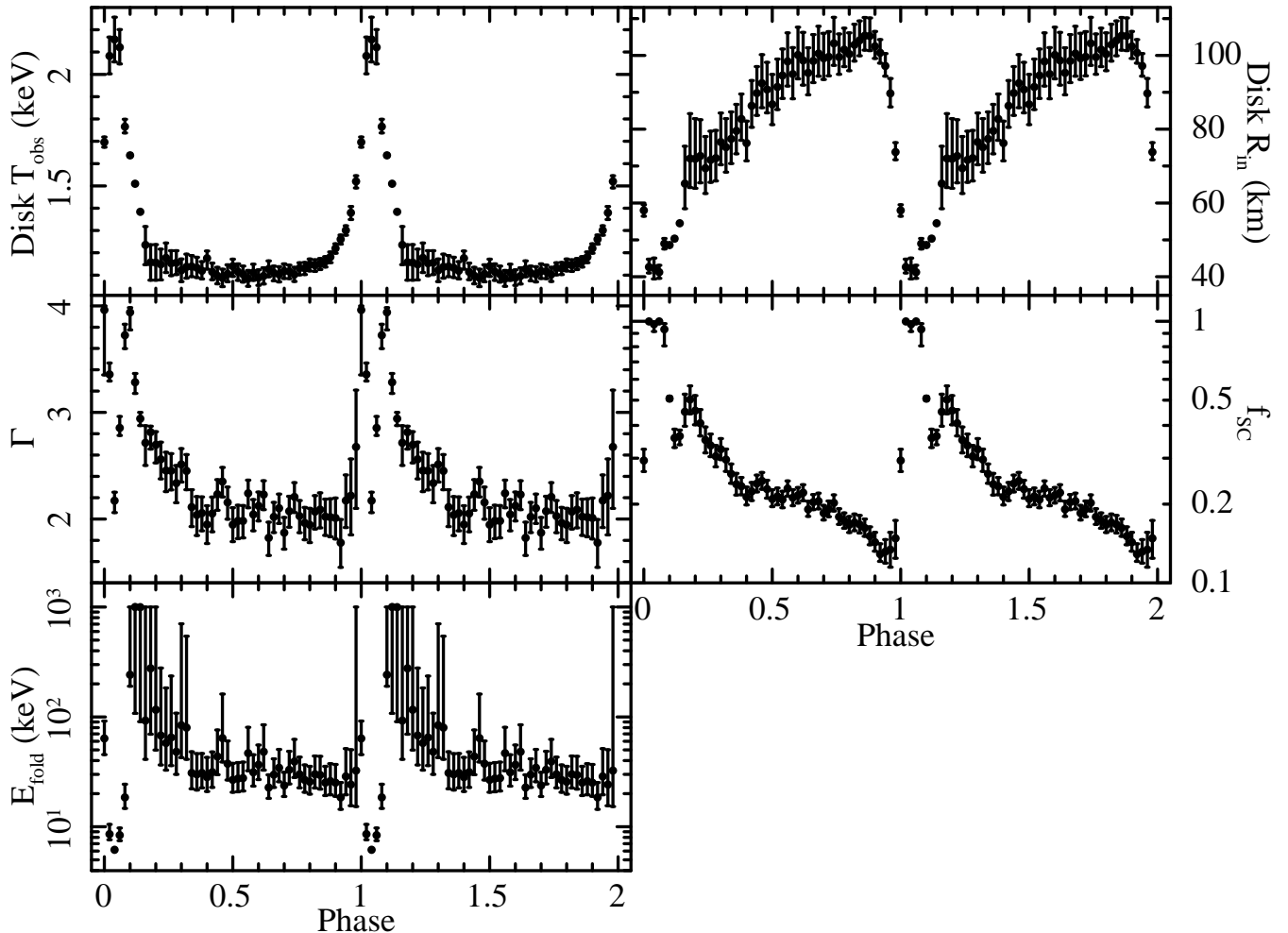


FIG. 7.— Model 1 fit parameters and  $1\sigma$  error bars as a function of phase for the PCA spectra (averaged over different PCU combinations). Two cycles are shown for clarity; since the average period is 50.33 seconds, each phase bin corresponds to roughly 1 second of real-time variability. The temperature and radius of the accretion disk vary significantly throughout the cycle, reminiscent of changes in the  $\kappa/\lambda$  states analyzed by Belloni et al. (1997b,a). Because `simpl` counts disk photons to create the power law ( $f_{\text{SC}}$ ), Model 1 uniquely tracks the disk parameters *prior* to Comptonization, i.e. scaling up the disk normalization by a factor  $1 - f_{\text{SC}}$ . See 4.1.1 for details of the model fits.

Meanwhile, the scattering fraction  $f_{\text{SC}}$  decreases slowly during the slow rise and reaches a minimum  $\sim 0.13$  near  $\phi = 0.95$ . Then, during the hard pulse at  $\phi \sim 0.06$ ,  $f_{\text{SC}}$  spikes sharply to 1; there is a second, broader peak with  $f_{\text{SC}} \sim 0.6$  during the hard X-ray tail (Fig. 7). We interpret this behavior as an indication that during the hard pulse, the X-ray spectrum is completely dominated by scattering and there is essentially no direct disk component. Still, the disk dominates the light during the soft pulse, contributing as much as 70% of the observed flux just before  $\phi = 0$ , and roughly 25% during the hard X-ray tail.

The high-energy cutoff exhibits similarly strong variations around the phase of the hard pulse. During most of the cycle,  $E_{\text{fold}}$  is steady around 30 keV, although the spectrum of the hard X-ray tail is effectively consistent with no cutoff, or with  $E_{\text{fold}} \lesssim 1$  MeV. But during the hard pulse,  $E_{\text{fold}}$  drops sharply to 6 keV. Thus Model 1 leads to the interpretation of the hard pulse as a period of very strong (i.e. Compton thick) scattering by relatively cool electrons.

The flux ( $F_{6.4 \text{ keV}}$ ) in the Gaussian emission line (see Section 5.2) declines very slowly for most of the cycle,

but peaks during the soft pulse. With the exception of this short pulse, the line flux is very strongly correlated with the line width  $\sigma_{6.4 \text{ keV}}$ , which varies between about 0.5 keV and 1.5 keV. The correlation coefficient for these two parameters is  $r = 0.88$ . At the *RXTE* spectral resolution, it is difficult to reliably decouple the variations in the line width and the line flux, so the true variability of the feature is unclear. The line is too broad to be observable in the *Chandra* HETGS spectrum. However, if we include only the phases of the cycle away from the pulses,  $\phi = 0.15 - 0.8$ , we find a moderate correlation between the line flux and the `simpl` scattering fraction ( $r \sim 0.63$ ). We will return to this in Section 5.2.

#### 4.1.2. Model 2: `nthcomp`

In the interest of quantifying the robustness of our results to the choice of hard X-ray component, we also explore the evolution of the disk with several prescriptions for Comptonization, including `compTT` and `nthcomp` (Zdziarski, Johnson, & Magdziarz 1996; Życki, Done, & Smith 1999). Here we discuss the results from our modeling with `nthcomp`. To use this model, we set the seed photon distribution to be a disk blackbody



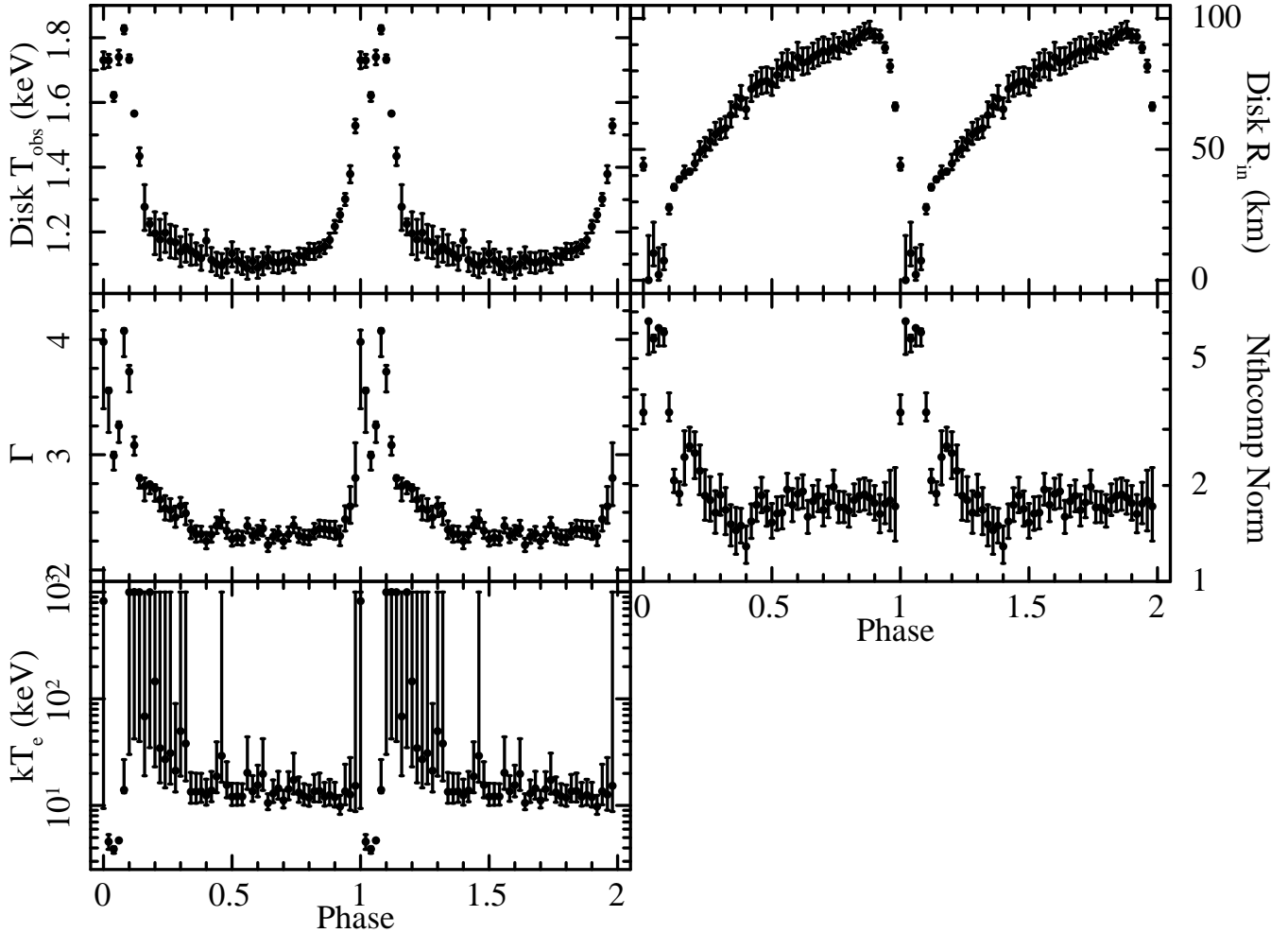


FIG. 8.— Model 2 fit parameters and  $1\sigma$  error bars as a function of phase for the PCA spectra (averaged over different PCU combinations). Two cycles are shown for clarity; since the average period is 50.33 seconds, each phase bin corresponds to roughly 1 second of real-time variability. The disk temperature and radius are very similar to those of Model 1. The `nthcomp` seed photon temperature is tied to the accretion disk temperature, so that both parameters are well-constrained even when the disk normalization goes to zero. See Section 4.1.2 for the details of Model 2.

and tie the seed temperature to the disk temperature. This allows the disk temperature to be well-constrained even when the disk normalization goes to zero (see below). The resulting variations are qualitatively very similar to those measured with `simpl`, and are shown in Figure 8. The overall goodness of fit is  $\chi^2_\nu = 1.09$ . The power law index  $\Gamma$  and the electron temperature  $kT_e$  are strikingly similar to the corresponding parameters in Model 1, and although the normalization of `nthcomp` is defined differently than  $f_{\text{SC}}$ , these two parameters also behave alike. See Table 1 for a comparison of the fit parameters at  $\phi = 0.06$ .

Still, there are several noticeable distinctions between Model 1 and Model 2, which are primarily related to the fact that with `simpl`, the photons in the hard X-ray component come directly from the disk component, while `nthcomp` treats them as distinct. For example, we find in Model 2 that our disk radii and temperatures are somewhat lower, peaking at approximately 100 km and 1.8 keV instead of 110 km and 2.2 keV. Furthermore, during the hard pulse, the spectrum is so completely dominated by the `nthcomp` component that the disk normalization (and radius) go to zero. This phenomenon is certainly

unphysical, so we ultimately prefer `simpl` (and its use of  $f_{\text{SC}}$  to track the pre-Comptonized disk) to `nthcomp` as a description of the spectrum.

Nevertheless, the strong changes in the accretion disk and Comptonization parameters around the hard pulse appear to lead to the same conclusion as Model 1. In both models, the hard pulse is characterized by strong scattering, a relatively steep photon index ( $\Gamma = 2.5$  in Model 1, 3.2 in Model 2), and a population of scattering electrons with significantly-reduced energy ( $E_{\text{fold}} = 6$  keV in Model 1,  $kT_e = 4\text{--}5$  keV in Model 2). These numbers are not characteristic of the canonical X-ray hard state. Therefore, while it is clear that Comptonization models do provide a good description of the X-ray spectrum, our findings here confirm our conclusion from Section 3.3 that it is difficult to interpret the hard pulse as a brief X-ray hard state.

#### 4.1.3. Model 3: Bremsstrahlung

We are now left with a small dilemma. The Comptonized disk models provide a very good statistical description of the phase-resolved X-ray spectra of the heartbeat state. However, several points indicate the possi-

TABLE 1  
X-RAY CONTINUUM PROPERTIES AT  $\phi = 0.06$  (HARD PULSE)

Parameter	Model 1	Model 2	Model 3
$R_{\text{in}}$ (km)	$41 \pm 2$	$< 12.4$	$22.1 \pm 0.4$
$T_{\text{obs}}$ (keV)	$2.12 \pm 0.08$	$1.74 \pm 0.02$	$2.19 \pm 0.03$
$\Gamma$	$2.86^{+0.11}_{-0.07}$	$3.29^{+0.03}_{-0.29}$	$> 3.2$
$f_{\text{SC}}$	$> 0.99$	...	$0.007^{+0.027}_{-0.004}$
$N_{\text{nthcomp}}$	...	$6.23^{+0.03}_{-0.76}$	...
$K_{\text{bremss}}$	...	...	$9.56 \pm 0.06$
$E_{\text{fold}}$ (keV)	$8.4^{+1.4}_{-0.9}$	...	...
$kT_e$	...	$4.70^{+0.14}_{-0.07}$	...
$kT_{\text{bremss}}$ (keV)	...	...	$6.38^{+0.05}_{-0.26}$
$F_{6.4 \text{ keV}}$	$0.027^{+0.008}_{-0.009}$	$0.012^{+0.006}_{-0.007}$	$0.051 \pm 0.008$
$\sigma_{6.4 \text{ keV}}$ (keV)	$< 1.0$	$< 1.2$	$0.8 \pm 0.2$
$\chi^2/\nu$	21.9/43	24.5/43	32.0/40

NOTE. — The hard pulse is the point of the  $\rho$  cycle that has the most unusual spectral and timing properties, and coincides with the most dramatic changes in the continuum parameters. It therefore provides an ideal contrast between our models. The values reported here are averages of the two PCU combinations; the individual errors (90% confidence ranges for a single parameter) have been added in quadrature with the standard deviation of the values for the two PCU sets.  $\chi^2$  is calculated for 56 data points.

ble presence of a second hard component in the X-ray spectrum. The most powerful argument in favor of such a component comes from the X-ray spectra themselves. For more than 70% of the cycle, both the photon index and the electron temperature are completely constant, and the scattering fraction varies smoothly. But these parameters change dramatically during the hard pulse and then return to “normal.” This suggests that there may be two geometrically-distinct sources of hard X-rays (one roughly constant and one variable). Additional evidence for a second component comes from the power density spectra (Section 3.3): during the hard X-ray tail and the beginning of the slow rise, the *rms* level, the shape of the PDS, and the evolution of the QPO frequency are all consistent with the properties of the hard-state-like dips in GRS 1915+105. These dips are known to be dominated by Compton scattering. The hard pulse (Fig. 2b), on the other hand, exhibits a dip in *rms* and there is no low-frequency QPO, which is typically associated with Compton-dominated intervals at high luminosity. This further indicates that the mechanism producing the hard X-rays during the hard pulse may be distinct from that in the hard X-ray tail and the slow rise. Finally, our timing analysis of 242 *RXTE* observations of the  $\rho$  state (Neilsen et al. 2011, in preparation) and the theoretical models of Nayakshin et al. (2000) and Janiuk & Czerny (2005) support the presence of a second component during the hard pulse that may be related to plasma ejections from the inner disk.

To test this idea, we replace the high-energy cutoff in Model 1 with a thermal bremsstrahlung component to represent the emission from this ejected plasma. The overall quality of the fit is comparable to the other models ( $\chi^2_\nu = 1.12$ ), but because *simpl* alone provides a decent fit outside the X-ray pulses, the hard component is occasionally over-determined. Nevertheless, this

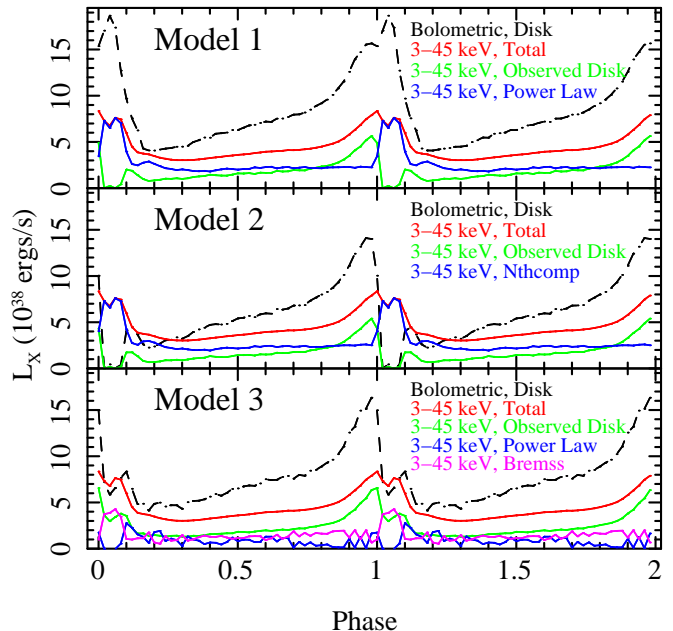


FIG. 9.— Luminosities of spectral components as functions of cycle phase. In the top panel, for Model 1, the bolometric disk luminosity (before scattering) is shown as a dot-dashed black line; we plot the 3–45 keV total, observed disk, and scattered (power-law) luminosities as red, green, and blue solid lines, respectively. The middle panel is the same but for Model 2, with the luminosity of the *nthcomp* component in blue. The bottom panel (Model 3) additionally shows the bremsstrahlung component in purple.

model presents a physically-interesting alternative to the Compton-dominated models, so we discuss it here briefly.

The accretion disk temperature and inner radius behave similarly to the parameters shown in Figure 7, although we find again that the disk normalization is smaller due to the presence of the bremsstrahlung component. But in light of the sudden changes in the hard X-ray components during the hard pulse in Models 1 and 2, we are primarily interested in the phase dependence of the bremsstrahlung normalization and temperature in Model 3. Here, we find a sharp spike in the bremsstrahlung normalization from  $K = 1 - 2$  at  $\phi = 0$  to a value of  $K = 9.56 \pm 0.06$  at  $\phi = 0.06$ . The normalization is given by

$$K = \frac{3.02 \times 10^{-15}}{4\pi D^2} \int n_e n_i dV, \quad (2)$$

where  $D$  is the distance to GRS 1915+015,  $n_e$  and  $n_i$  are the electron and ion number densities, and  $V$  is the emitting volume. The bremsstrahlung temperature during this spike is  $kT_{\text{bremss}} \sim 5 - 7$  keV, which is consistent with the evolution of the electron temperature in Models 1 and 2. Although the exact physical interpretation of the hard X-ray component varies from model to model, all three models require the sudden appearance of a new population of electrons during the hard pulse, which coincides with dramatic changes in the accretion disk. These electrons are cooler than typical coronal electrons, but warmer than the disk.

For comparison, we show the luminosities of the X-ray continuum components in Figure 9, from which several points are immediately clear. First, the hard X-ray luminosity is relatively steady in all three models, with the exception of the hard pulse, which is scattering dom-

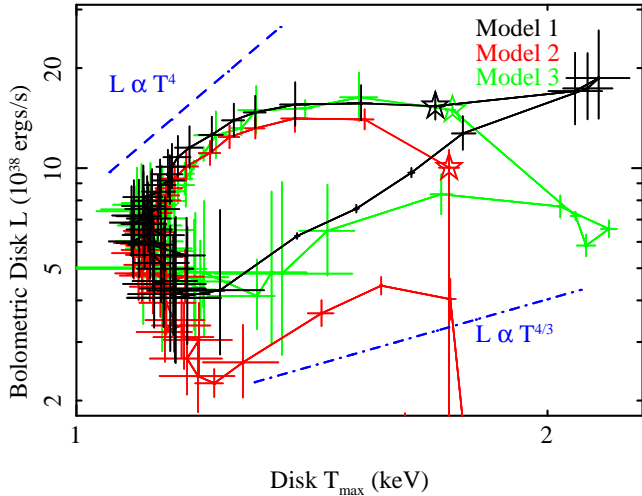


FIG. 10.— Accretion disk bolometric luminosity versus temperature for our continuum models (Model 1 in black, Model 2 in red, Model 3 in green). We use a star to mark the location of  $\phi = 0$  for both curves; motion around the loop is clockwise. We also overplot dashed and dot-dashed blue lines of  $L \propto T^4$  and  $T^{4/3}$ , which are expected if the disk radius or the accretion rate is constant, respectively. Note that we have cut off Model 2 (`nthcomp`) where the disk luminosity goes to zero.

inated in Models 1 and 2 but 56% bremsstrahlung in Model 3. Second, the hard X-ray tail ( $\phi = 0.15 - 0.3$ ) is also dominated by scattering (here the disk component constitutes  $\lesssim 30\%$  of the light in all models). Finally, we can see that in all models, just before  $\phi = 0$  the bolometric disk luminosity (see also 4.1.4 for details) reaches 80-90% of the Eddington luminosity for GRS 1915+105 (a  $14 M_{\odot}$  black hole;  $L_{\text{Edd}} = 1.8 \times 10^{39}$  ergs  $\text{s}^{-1}$ ). Model 1 actually tops out at  $1.03L_{\text{Edd}}$ .

#### 4.1.4. Disk Variations and the Accretion Rate

The most obvious feature of our fits to the heartbeat state X-ray continuum is the strong variability in the temperature and inner radius of the accretion disk. Before turning to a theoretical interpretation of the  $\rho$  cycle (Section 5), we assess the implications of our continuum fits for the mass accretion rate onto the black hole.

Given the color correction factor  $f$  and the measured inner radius and temperature of the disk, we can calculate the disk mass accretion rate using equation (4) of Zimmerman et al. (2005):

$$T_{\text{obs}} = \frac{f}{2.05} \left( \frac{3GM\dot{M}}{8\pi R_{\text{in}}^3 \sigma} \right)^{1/4}, \quad (3)$$

where  $G$  is the gravitational constant,  $M$  is the black hole mass, and  $\sigma$  is the Stefan-Boltzmann constant. We evaluate the accretion rate as a comparative scale, noting that the absolute value is quite uncertain, and that we assume no changes in spectral hardening or the radiative efficiency of the disk. All three models give very similar mass accretion rates and bolometric luminosities. We find that  $\dot{M}$  peaks just before the spike in the disk temperature at  $\phi = 0$ , at a value  $\dot{M} \lesssim 1.5 \times 10^{19}$  g  $\text{s}^{-1}$ . After the peak, the mass accretion rate drops sharply to  $\dot{M} \sim (1 - 3) \times 10^{18}$  g  $\text{s}^{-1}$ . For all models the evolution of  $\dot{M}$  is similar to that of the bolometric disk luminosities (Figure 9).

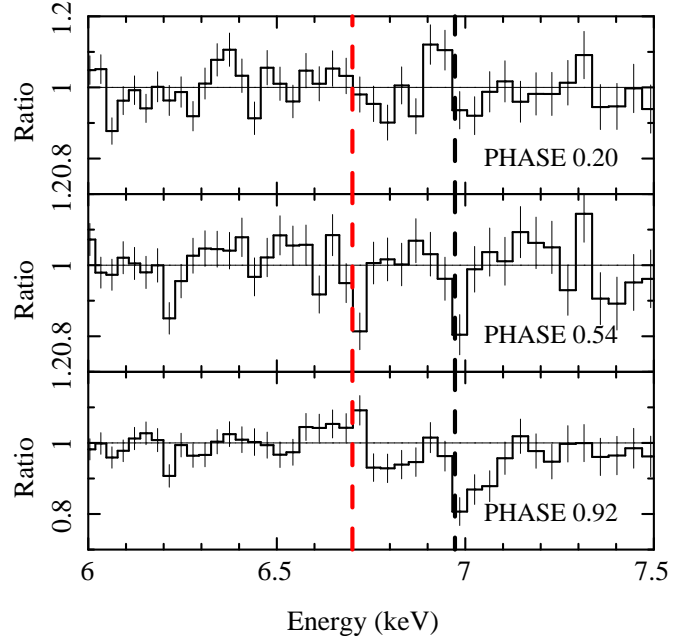


FIG. 11.— HETGS model/data spectra for three different phases of the heartbeat cycle with the rest energies of Fe XXV ( $\text{He}\alpha$ :  $1s^2 - 1s2p$ , 6.7 keV) and Fe XXVI ( $\text{Ly}\alpha$ :  $1s - 2p$ , 6.97 keV) marked in red and black, respectively. At  $\phi = 0.2$ , near the cycle minimum, the iron absorption lines are weak. At  $\phi = 0.54$ , we detect noticeable features from Fe XXV and Fe XXVI, both blueshifted by  $\sim 500$  km  $\text{s}^{-1}$ . The feature at 6.2 keV may be Mn XXIV  $\text{He}\alpha$  or some other Doppler-shifted absorber. At  $\phi = 0.92$ , the Fe XXV line is gone, but there is some evidence for faster ( $\sim 5000$  km  $\text{s}^{-1}$ ) and broader iron absorption in the Fe XXVI line profile.

The evolution of the accretion disk component can also be seen in Figure 10, where we plot its bolometric luminosity versus its temperature. During the  $\rho$  cycle, GRS 1915+105 traces a clockwise loop in the  $L - T$  plot. In Models 2 and 3, the loop is distorted because of the competition between the disk, `nthcomp`, and bremsstrahlung components, but the behavior is otherwise similar. Although we calculate each point on the plot ala Zimmerman et al. (2005):

$$L = 73.9\sigma \left( \frac{T_{\text{obs}}}{f} \right)^4 R_{\text{in}}^2 = 73.9\sigma T_{\text{obs}}^4 \frac{N_{\text{disk}} D^2}{\cos i}, \quad (4)$$

there is essentially no interval longer than a few seconds over which  $L \propto T^4$ . After  $\phi = 0$ , which is marked with a star, the disk moves rapidly from its moderate temperature, high luminosity state through a high temperature, moderate luminosity state ( $\phi \sim 0.06$ ) to a low temperature, low luminosity state ( $\phi \sim 0.2$ ). After the minimum, the luminosity rises at roughly constant temperature (in our nomenclature, this interval is the slow rise; see Fig. 2b). For reference, we overplot lines of  $L \propto T^4$ , which results from a constant inner disk radius, and  $L \propto T^{4/3}$ , which is expected for a constant accretion rate. These lines broadly match the evolution of  $L$  going into and out of the slow rise. We will return to this plot, its interpretation, and the question of the mass accretion rate in Section 5.

#### 4.2. Chandra HETGS

While the *RXTE* PCA provides high S/N broadband X-ray spectra for measurements of the continuum, the

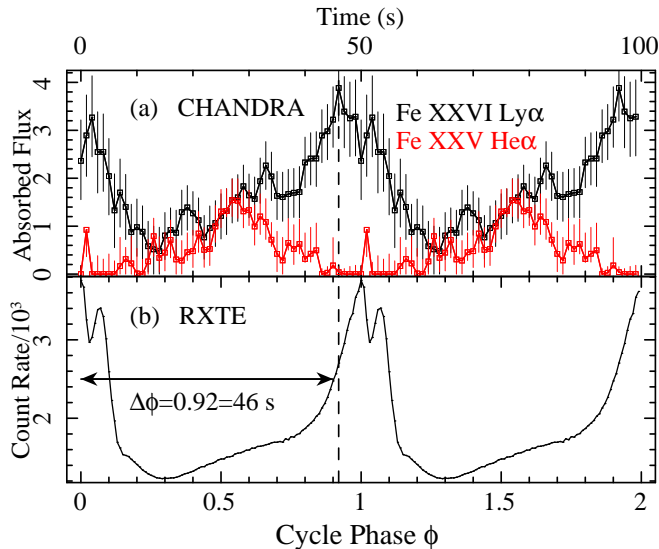


FIG. 12.— (a) Measured flux (in units of  $10^{-3}$  photons  $s^{-1}$   $cm^{-2}$ ) in the Fe XXV (red) and Fe XXVI (black) absorption lines as a function of  $\rho$  cycle phase. The H-like iron line clearly tracks the X-ray continuum, although the peak line flux follows the peak X-ray luminosity with a delay  $\Delta\phi = 0.92 \approx 46$  seconds. In contrast, the He-like line only appears briefly, growing in strength with Fe XXVI until  $\phi \sim 0.54$ , where it starts to fade. (b) The full band *RXTE* PCA phase-folded lightcurve, for ease of tracking changes in the absorption lines observed with *Chandra* (top panel).

*Chandra* HETGS provides an excellent high-spectral-resolution characterization of the observed narrow lines in the soft X-ray band that is ideal for studying the accretion disk wind and its dynamical evolution.

One of the most significant challenges for fast phase-resolved grating spectroscopy is choosing time and phase intervals to maximize the detectability of interesting features and their possible variations. For ease of comparison with the PCA spectra, we restrict our attention here to the  $\sim 20$  ks of the *Chandra* observation that bracket the *RXTE* data. This choice maximizes the S/N in the Fe XXV line, which increases over the course of our observation, relative to Fe XXVI (see Section 5.3.4). For our phase-dependent spectral analysis, we extract 50 HEG spectra evenly spaced in phase. In order to achieve sufficient S/N, we set the phase width of each spectrum to  $\Delta\phi = 0.2$ . This is essentially a sliding box window, so there is some overlap between consecutive spectra, but as shown by Schulz & Brandt (2002), this method is quite suitable for line variability studies. As discussed in Section 2.1, because of calibration uncertainties we model the *Chandra* X-ray continuum with a polynomial fit (instead of the physical models of Section 4.1). Polynomials accurately characterize the local continuum, so they effectively isolate narrow absorption lines. See Figure 11 for three example residual spectra.

A complete search for variable features at all velocities and ionization levels with any arbitrary phase dependence is beyond the statistical scope of this paper. Since we are mainly interested in the known accretion disk wind in GRS 1915+105 (Lee et al. 2002; Paper I), we focus on the observed narrow iron absorption lines with velocities ranging from  $\sim 500$  to  $2000$   $km\ s^{-1}$  (see, e.g. the middle panel of Figure 11). We detect both Fe XXVI (Ly $\alpha$ : 1s – 2p, 6.97 keV) and Fe XXV (He $\alpha$ : 1s<sup>2</sup> – 1s2p, 6.7 keV). We use Gaussian fits to measure the pa-

rameters of these iron absorption lines at each phase (see Table 2). To decouple our results from possible variations in the wind dynamics, which could manifest as changing line widths and thus affect the apparent line flux, we fix the intrinsic line width at  $200$   $km\ s^{-1}$ . This is a typical orbital speed in the outer disk, and matches the turbulent line width found by Ueda et al. (2009) in their study of the  $\phi$  state. When we detect both Fe XXV and Fe XXVI, we can fit for a 90% confidence upper limit on the line width of  $800$   $km\ s^{-1}$ .

Finally, we note the possible presence of additional lines that vary with phase, including a line at 6.2 keV that may be Mn XXIV He $\alpha$  and an unidentified feature at 4.29 keV. Without secure identifications it is unclear if they are part of the iron absorber or if they represent a different dynamical component, such as an acceleration zone of the wind or a signature of infall. Both have maximum fluxes around  $2.0 \pm 0.5$  photons  $s^{-1}$   $cm^{-2}$ ; the corresponding equivalent widths are 2.5 eV and 6.4 eV, respectively. Since we cannot clearly identify their origin we do not consider them further here, beyond noting that their phase dependence is somewhat similar to that of the iron absorber.

It is clear from both Table 2 and Figure 11 that the ionization parameter  $\xi$  of the wind changes substantially during the cycle. Table 2 shows that Fe XXV and Fe XXVI peak with similar equivalent widths at very different phases ( $\phi = 0.54$  vs.  $\phi = 0.92$ ), while a comparison of the middle and bottom panels of Figure 11 shows that the Fe XXVI absorption line is strong even when the Fe XXV line has disappeared. In the rest of this section, we focus on these two later phases as representative of the variations in disk wind absorption in this state.

This ionization evolution is even more obvious in Figure 12. The Fe XXV absorption line appears to track the Fe XXVI line in the interval  $\phi = 0.2 - 0.54$ , but it fades rapidly outside this interval and is not significantly detected for the rest of the cycle. The Fe XXVI absorption line, however, continues to grow until  $\phi = 0.92$ . The peak flux in this line is more than twice that measured from the average spectrum; Monte Carlo simulations indicate that this increase is significant at 96% confidence.

It is also evident in Figure 12 that the Fe XXVI absorption line evolves similarly to the PCA count rate. Under the assumption that the line variability is a response to the X-ray continuum impinging on the wind, it appears that the peak line flux follows the X-ray flux with a delay  $\Delta\phi \approx 0.92 = 46$  seconds. This is actually rather long: the semimajor axis of GRS 1915+105 is  $a \sim 250$  lt-s (Greiner, Cuby, & McCaughrean 2001), and previous estimates have placed the wind near  $r \sim 10$  lt-s from the black hole (Lee et al. 2002; Ueda et al. 2009; Paper I). It may then be reasonable to suspect that  $\Delta\phi$  is mainly due to continued increases in the ionization of the absorbing gas. We will show in Section 5.3 that changes in the gas density are also important.

Additionally, we note that our measurements of the absorption line centroids provide marginal evidence for variations in the blueshift of the wind during the cycle. At  $\phi = 0.54$ , we detect Fe XXVI at  $v \sim -430^{+390}_{-750}$   $km\ s^{-1}$ ; by  $\phi = 0.92$ , the velocity has increased to  $v \sim -1600^{+360}_{-50}$   $km\ s^{-1}$ . This apparent acceleration is significant at 96% confidence, and it occurs in combination with the ap-

TABLE 2  
X-RAY ABSORPTION LINES IN THE  $\rho$  STATE OF GRS 1915+105

Phase	Line	$E_0$ (keV)	$E_{\text{obs}}$ (keV)	$\Delta v_{\text{shift}}$ (km s $^{-1}$ )	Flux	$W_0$ (eV)
0.20	Fe XXVI Ly $\alpha$	6.966	$7.01^{+0.02}_{-0.01}$	$-1700^{+500}_{-1000}$	< 1.6	> -8.6
	Fe XXV He $\alpha$	6.700	6.711 <sup>a</sup>	-490 <sup>a</sup>	< 0.5	$-0.1^{+0.1}_{-2.6}$
0.54	Fe XXVI Ly $\alpha$	6.966	$6.976^{+0.018}_{-0.009}$	$-430^{+390}_{-750}$	$1.5 \pm 0.5$	$-11.2^{+3.5}_{-3.4}$
	<b>Fe XXV He<math>\alpha</math></b>	6.700	$6.711^{+0.010}_{-0.008}$	$-490^{+370}_{-420}$	$1.5^{+0.4}_{-0.3}$	$-10.1^{+2.2}_{-3.0}$
0.92	<b>Fe XXVI Ly<math>\alpha</math></b>	6.966	$7.004^{+0.001}_{-0.008}$	$-1610^{+360}_{-50}$	$3.9 \pm 0.7$	$-14.1^{+2.5}_{-2.4}$
	Fe XXV He $\alpha$	6.700	6.711 <sup>a</sup>	-490 <sup>a</sup>	< 0.1	> -0.5

NOTE. — Errors quoted are 68% confidence ranges for a single parameter. Phase: line parameters are reported for three different phases of the cycle;  $E_0$ : rest energy;  $E_{\text{obs}}$ : measured energy;  $\Delta v_{\text{shift}}$ : measured Doppler velocity; Flux: measured absorbed line flux in units of  $10^{-3}$  photons s $^{-1}$  cm $^{-2}$ ;  $W_0$ : line equivalent width;  $\phi_{\text{max}}$ : phase of maximum line flux. Boldface indicates the phase of maximum flux for that ion.

<sup>a</sup> Since the Fe XXV line is not detected at this phase, we fix its energy at the value measured at  $\phi = 0.54$  to place limits on the line flux and equivalent width.

pearance of a blue wing to the Fe XXVI profile (see Fig. 11). We then take the velocity and line width as some evidence of variability in the dynamics of the disk wind. In Section 5.3, we discuss the photoionization evolution, dynamics, and the 46-second delay in the context of wind formation scenarios and the disk-wind-jet connection.

## 5. DISCUSSION

In this section, we explore the significance of our results from Sections 3 and 4. Specifically, we will address our findings of (1) strong, fast variations in the inner radius of the accretion disk, (2) bremsstrahlung emission during the hard pulse, and (3) clear changes in the absorption lines from the accretion disk wind on timescales of 5 seconds.

While strong variations in the X-ray spectrum of GRS 1915+105 are routinely observed, the magnitude and short timescale of the spectral variability in the heartbeat state bears repeating, especially given its cyclic nature. In the rising phase of the cycle, the bolometric disk luminosity changes from about  $(5 \text{ to } 16) \times 10^{38}$  ergs s $^{-1}$  in roughly 35 seconds; during the decay phase, the X-ray luminosity decreases by as much as  $\dot{L}_X \lesssim 5 \times 10^{38}$  ergs s $^{-2}$ . In other words, we find that the black hole halts a burst reaching  $\sim 80 - 90\%$  of its Eddington luminosity in just a few seconds. As discussed in Section 4, the luminosity variations are associated with substantial changes in the inner radius and temperature of the accretion disk.

The physical changes in this bizarre oscillation are represented in the phase variation of the X-ray continuum, fluorescent emission lines, and the hot iron absorption lines of the accretion disk wind. In the following subsections, we discuss our results on phase-resolved spectra and power spectra to understand the origin, dynamics, and accretion geometry of the  $\rho$  state and to explore in detail the apparent coupling between the accretion disk wind and the X-ray oscillation. *We describe our model for the physics of the heartbeat state, starting with variations in the accretion rate in the inner disk, and tracing their influence on the accretion dynamics all the way to the outer edge of the disk.*

### 5.1. X-ray Continuum

#### 5.1.1. $\dot{M}$ Variations and Z Source-like Behavior

The most obvious properties of the heartbeat state (based on our X-ray continuum fits) are the observed strong variability in the luminosity, temperature, and inner radius of the accretion disk (Figs. 7–10). Specifically, our analysis shows that during the slow rise, the disk radius gradually grows, then drops sharply and rebounds during the X-ray peaks. Meanwhile, the disk temperature appears constant and then spikes rapidly.

Lin, Remillard, & Homan (2009, hereafter LRH09) discovered similar variations in the radius, temperature, and luminosity of the accretion disk in the accreting neutron star XTE J1701-462 as it evolved from a Z-source to an atoll source. Z sources are accreting neutron stars that display three branches in the shape of a “Z” in their color-color diagrams. LRH09 found that in the ensemble of observations in the vertex between the flaring branch and normal branch, the inner radius of the disk increased with luminosity above  $L \sim 0.2L_{\text{Edd}}$ , while the disk temperature remained roughly constant. They interpreted this result as an indication of a local Eddington limit (Fukue 2004; Heinzeller & Duschl 2007) in the inner disk. Local Eddington effects arise because the radiation forces and gravitational forces depend differently on radius in thin disks, so that there exists a critical radius where radiation pressure can truncate the disk. Inside this critical radius, a significant fraction of the disk is expelled by radiation pressure. The resulting spectrum is the same as that of a standard thin disk for energies  $E \gtrsim k_B T_{\text{crit}}$ . It is possible that the same process is at work during the slow rise of the  $\rho$  cycle in GRS 1915+105, i.e. when the radius increases with luminosity at roughly constant  $T$  (Fig. 10).

LRH09 also showed that on the XTE J1701-462 flaring branch, the luminosity is proportional to  $T^{4/3}$ , which is expected if the inner radius of the disk changes while the accretion rate remains constant. They concluded that the flaring branch is an instability in which the disk temporarily slips inwards but is quickly driven back to the equilibrium position seen at the vertex position on that



same day. In their interpretation, this equilibrium position is set by the local Eddington limit. For comparison, we plot a line of  $L \propto T^{4/3}$  in Figure 10. It can be seen that in GRS 1915+105, the disk very roughly approximates this scaling as it both approaches and exits the slow rise of the  $\rho$  cycle. We also show  $L \propto T^4$ ; the two lines bracket the behavior of the accretion disk during the  $\rho$  cycle. These rough scalings seem to indicate that some changes in the disk may occur at  $\sim$ constant accretion rate, especially after  $\phi = 0$ .

Thus, mapping LRH09’s prescription for neutron stars onto GRS 1915+105, we can understand the gradual increase in the disk radius during the slow rise of the heartbeat state as a local Eddington phenomenon (our measured radii and temperatures are consistent with those predicted by Fukue 2004). The disk slowly expands with an increasing accretion rate. After the accretion rate reaches a maximum the disk first falls in at  $\sim$  constant accretion rate and then cools rapidly while the accretion rate drops, setting the stage for the next cycle. It should be noted that the analogy between the XTE J1701-462 lower vertex/flaring branch and the  $\rho$  cycle is not exact, since the variations in GRS 1915+105 are much faster, and XTE J1701-462 does not trace out a loop in the  $L-T$  diagram. Furthermore, only GRS 1915+105 shows the rapid catastrophic changes seen in the disk and the accretion rate around  $\phi = 0$ .

Nevertheless, it is very exciting to see such similar accretion disk behavior between a neutron star system and a black hole system; the commonalities suggest that the  $\rho$  cycle may share or mimic some properties of a Z source. This particular comparison seems reasonable, since Z sources are known for high accretion rates (see LRH09 and references therein), and GRS 1915+105 may have the highest accretion rate of any known black hole transient. These similarities also support the conclusion of Done, Wardziński, & Gierliński (2004) that GRS 1915+105 may be unique merely for its high accretion rate.

### 5.1.2. On the Role of Radiation Pressure

Our interpretation that the local Eddington limit in the inner accretion disk may produce the slow rise during the  $\rho$  cycle (see Section 5.1.1) poses an intriguing question as to the role of radiation pressure in the heartbeat state. We now have claims of two very different radiation pressure phenomena in the  $\rho$  state: a local Eddington limit and (historically) the Lightman-Eardley radiation pressure instability (RPI). The RPI is commonly invoked, with some success, to explain the strong limit cycle oscillations in GRS 1915+105 (TCS97; Nayakshin et al. 2000, hereafter NRM00; Janiuk & Czerny 2005, hereafter JC05). These processes are physically independent but not necessarily conflicting. Here we consider the question: what is the true role of radiation pressure in the  $\rho$  state? Does it produce limit-cycle oscillations by making the disk (in contact at constant  $R_{\text{in}}$ ) thermally/viscously unstable, or does it actually push out the inner radius of the disk over timescales of  $\sim 25 \text{ s} \approx 4000$  dynamical times? Or are some elements of both models required to explain the observations? To answer this question, we need to understand how the observed changes in the radius, temperature, and luminosity of the accretion disk might be

related to these physical mechanisms.

For the local Eddington limit,  $R_{\text{in}}$  increases with  $L$  at constant  $T$ . For half of each observed  $\rho$  cycle (the slow rise; Fig. 2b), the disk luminosity and radius appear to grow at  $\sim$ constant  $T$ . Alone, however, a local Eddington limit cannot produce an oscillation or a loop in the  $L-T$  diagram. Some other mechanism is required to cyclically vary the accretion rate for a complete description of the heartbeat state.

The question is more subtle as it relates to the RPI. Does the RPI act in concert with a local Eddington limit to produce the  $\rho$  state, or can it mimic an interval of increasing  $R_{\text{in}}$  at constant  $T$ ? Since time-dependent disk simulations of the RPI (e.g. NRM00 and JC05) have not produced synthetic spectra, the question is also difficult to answer. For preliminary considerations, we examine the dynamics of the accretion disk in their simulations.

Physically, the RPI occurs when the inner disk becomes unstable due to radiation pressure. This drives a limit cycle involving an oscillation of the local accretion rate in the inner disk. This can be interpreted as a ‘density wave’, which originates around  $R_{\text{dw}} = 20 - 30 R_{\text{g}}$ . Here  $R_{\text{g}}$  is the gravitational radius (21 km for GRS 1915+105). As the density wave moves through the disk, it partially evacuates a gap in the disk. Inside and outside the gap, the disk surface density is enhanced (see Figure 4 in both NRM00 and JC05). The inner density enhancement peaks around  $R = 5 R_{\text{g}} \approx 105 \text{ km}$ . The similarity of this estimate to our measured radii is striking. During the decay of the cycle, this excess density moves inwards quickly (and our measured radii decrease sharply). These results provide a hint as to why the apparent disk radius might change rapidly in the pulses.

It is unclear, however, if the RPI can mimic our observation of increasing  $R_{\text{in}}$  at constant  $T$  during the slow rise. Our local Eddington interpretation implies that the true edge of the disk moves outwards with  $L$ , while NRM00 and JC05 have  $R_{\text{in}}$  fixed at  $2 R_{\text{g}}$ . On the other hand, the disk surface density and temperature are increasing and decreasing functions of radius, respectively, and both groups find a short hot state and an extended ‘cold’ state. For these reasons, it seems potentially possible for their time-dependent thin disk models to mimic an expanding-radius disk at constant  $T$ .

Thus the role of radiation pressure in the heartbeat state requires some additional model analyses. A local Eddington limit in the disk does a good job explaining the slow rise, but cannot explain the pulses or the existence of an oscillation. The RPI is a viable explanation for the oscillation, but it is unclear if it can either act alone or jointly with the local Eddington limit to reproduce our observations of the slow rise. Future time-dependent disk simulations will be able to resolve this issue by calculating model spectra that can be compared with the observations. For now, it seems that our observed disk radii and temperatures provide some support for both the RPI and a local Eddington limit at work in GRS 1915+105.

### 5.1.3. Ejections, Jets, and the Fate of the Inner Disk

Another exciting question posed by the observed rapid oscillations in the radius, temperature, and mass accretion rate in the disk concerns the ultimate fate of the excess material in the inner disk. Does it simply fall into

the black hole, or is it ejected from the inner disk and therefore potentially observable? We have not directly observed any ejection events, but the mysterious hard pulse in the X-ray lightcurve still lacks a satisfying interpretation. It is even peculiar theoretically, since RPI simulations produce only single-peaked cycles. Is this short burst of hard X-rays related to the ejection of material from the inner disk, or does it have an explanation in terms of standard black hole states?

The association of the hard pulse with a typical soft-to-hard state transition appears to be ruled out, since the spectral and timing properties of the hard pulse are not remotely consistent with typical hard states for either GRS 1915+105 or black hole binaries in general. That is, although we are able to successfully model its X-ray spectrum with disk/Comptonization models, the resulting parameters are inconsistent with the canonical hard state, and imply the sudden appearance of a low-temperature, high-optical-depth cloud of electrons ( $\tau \sim 5$  with `nthcomp`).

Before going ahead, we may ask if the appearance of these cooler electrons can be explained simply by an increase in their cooling rate. If synchrotron cooling is important, additional cooling could be accomplished by an increase in the electron density or magnetic field strength. If inverse Compton cooling dominates, then an increase in cooling could result from the observed increase in the X-ray flux or from an increase in the electron density. Detailed radiative transfer calculations would be necessary to determine the energetics precisely, but it is unclear in the Compton cooling case why the cooling is abrupt, while the flux changes smoothly. The simplest explanation in both cases is a sudden increase in the electron density. This justifies our use of a bremsstrahlung component to model the hard pulse, and provides us with an observational basis for discussing plasma ejections from the inner disk.

Additional support for plasma ejections comes from the theoretical work of NRM00 and JC05, who found that the X-ray states of GRS 1915+105 are reproduced with higher fidelity when ejection processes are included. NRM00 allowed a fraction of the total accretion power to be channeled into a jet with Lorentz factor  $\gamma \sim 3$ . JC05, modeling the  $\rho$  state specifically, allowed the disk to evaporate into the corona at the peak of the cycle.

It should be noted that these models (see also Janiuk et al. 2000) produce plasma ejections when the X-ray luminosity is greatest, and are therefore at odds with the conclusions of Klein-Wolt et al. (2002), who argued that jet production is essentially a continuous process that occurs during hard faint intervals (State C in the classification of B00). However, the  $\rho$  state is only known to exhibit low-level radio emission, and it is unclear if this is a ‘baby’ jet with a short duty cycle or some other stable but faint radio activity. Thus there may be no observational conflict with Klein-Wolt et al. (2002) for the  $\rho$  state. Future high time-resolution radio/X-ray observations (e.g. with the EVLA and *Chandra*) should probe the precise nature of the radio emission in such states.

In any case, both groups predict plasma ejections near  $\phi = 0$ , and our models implies the sudden appearance of some cold plasma around the same phase. With the reasonable assumption that these two points are

related, we proceed to estimate how much material is ejected from the disk. For this, we can use equation (2), which relates the bremsstrahlung normalization to the volume and electron density in the emitter. Because the bremsstrahlung pulse begins just after the drop in  $R_{\text{in}}$  at  $\phi \sim 0$ , we assume that  $R_{\text{bremss}} \sim \max(R_{\text{in}}) \sim 97$  km, so that the emitting volume is  $V_{\text{max}} \sim 4 \times 10^{21}$  cm<sup>3</sup>. In other words, we assume that some bremsstrahlung-emitting material is ejected from the inner disk, filling a sphere of radius 97 km. Assuming the particle density is constant over the sphere and that the material is fully ionized (with ISM abundances from Wilms et al. 2000), we find an implied ion density  $n_i \sim 10^{20}$  cm<sup>-3</sup> and ion mass  $m_i \sim 10^{18}$  g. For a Shakura-Sunyaev disk with  $\dot{M} \sim 10^{19}$  g s<sup>-1</sup>, the disk mass interior to 97 km is of order  $10^{21}$  g,  $\gtrsim 1000$  times larger than the mass of this bremsstrahlung cloud. Since JC05 argued that as much as 10% of the disk accretion rate may evaporate into the corona, our requirement that 0.1% of the disk mass contribute to the bremsstrahlung pulse seems reasonable.

Also of interest is the possible production of a collimated jet at some point in the  $\rho$  cycle. In Section 3.3, we considered the extent to which the X-ray minimum of the  $\rho$  state, or even the slow rise, could be considered a hard state, with the purpose of identifying those phase intervals where we might expect to see some signatures of jet production. Our examination of the phase-dependent PDS and X-ray continuum indicates that the end of the hard X-ray tail,  $\phi = 0.26 - 0.36$ , has timing and spectral properties that are consistent with an X-ray hard state. Thus if there is any jet activity, we might expect it to have a duty cycle of order 10%. In this window around the count rate minimum, a hard state (and jet) may temporarily coexist with the disk. This conclusion is particularly interesting in light of the possibility of strong synchrotron cooling during the hard pulse, but a radio detection of a synchrotron spectrum would be required to verify and connect these two phenomena.

Previously, we reported the Ryle telescope radio flux near this observation to be  $S_{15\text{GHz}} \lesssim 5$  mJy (Pooley & Fender 1997; Neilsen & Lee 2009), which is comparable to the sensitivity of the Ryle telescope. Thus we cannot draw any robust conclusions about a jet. We note, however, that this is averaged over nearly a full cycle; if the actual radio flux is close to this upper limit, then the ‘true’ jet strength could be an order of magnitude higher. This would be typical for a  $\chi$  state jet in GRS 1915+105 (Fender et al. 1999; Klein-Wolt et al. 2002). Since a short-lived jet is plausible, future sensitive radio observations of the  $\rho$  state may place strong constraints on jet evolution around black holes.

To summarize, it appears that our Comptonized disk plus bremsstrahlung model leads to a physically-sensible observational interpretation of the  $\rho$  state in the context of plasma ejections. We find that the double-peaked X-ray lightcurve is the result of two processes: (1) large, cyclic variations in the mass accretion rate in the inner disk, leading to an increase in the disk temperature (the soft pulse), and (2) the ejection/evaporation of a small fraction of the inner disk, which produces a brief burst of bremsstrahlung as it propagates into the corona (the hard pulse). The hard X-ray emission could also simply be scattering in a Compton-thick cloud, but the ap-

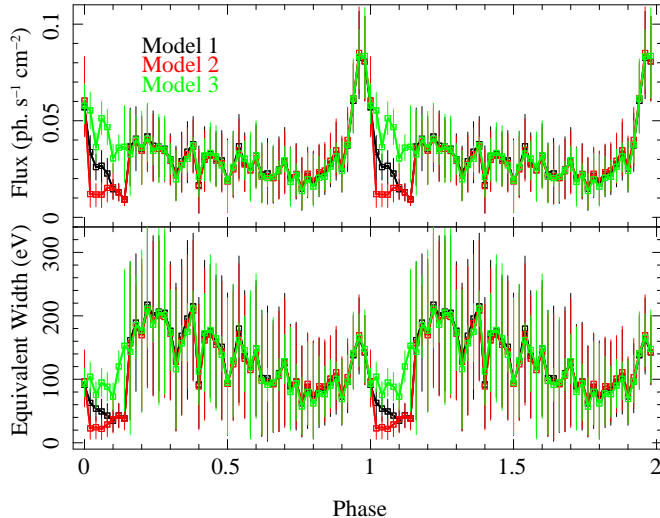


FIG. 13.— Flux (top) and equivalent width (bottom) of the broad iron emission line as a function of phase. The line flux is roughly constant during most of the cycle and spikes during the two pulses, while the equivalent width oscillates slowly.

pearance of this cloud is still best explained by material evaporating from the disk. This “steam” from the disk does not qualify as a jet, but it is nevertheless an exciting signature of plasma ejections during the heartbeat cycle.

### 5.2. Iron Emission Line

Here we briefly consider the broad iron line seen in our *RXTE* spectra (Figure 13). In our models, the line flux slowly decreases for most of the cycle and the equivalent width oscillates slowly, spiking during the soft pulse. Models 1 and 2 show a dip in the line strength during the hard pulse, but the reality of this feature is unclear. In the standard interpretation (Fabian et al. 1989; Matt, Fabian, & Ross 1993; Reynolds & Nowak 2003, and references therein), the broad line is a reflection feature from the inner accretion disk. As shown in Section 4.1, the innermost regions of the disk fluctuate cyclically during the  $\rho$  state, so the fact that the line flux is almost constant indicates that some geometrical effects from the oscillation may be influencing the illumination of the disk. For example, the increase of the disk scale height with luminosity may shield outer regions of the inner disk from some of the X-ray luminosity, allowing the reflected line flux to stay the same.

On the other hand, if the line originates at the inner edge of the disk, then the constant line flux might be caused by a combination of increased illumination and decreased reflecting area. We note that the line equivalent width looks rather like the `simpl` scattering fraction, so it seems likely that the changes in the hard X-ray component are literally reflected in the iron line. But without detailed theoretical models of the disk spectrum and the iron line profile, a robust determination of its location is not possible. Thus it would be difficult to use this broad line to place a constrain on the black hole spin. In other states like the  $\chi$  state, where the X-ray variability and its effects on the disk structure are not so important, estimates of the spin parameter  $a_*$  may be both more feasible and more meaningful (Martocchia et al. 2002; Blum et al. 2009).

### 5.3. Accretion Disk Wind

One of the main goals of this work, as a follow-up to our discovery of a wind-jet interaction in Paper 1, is to understand the complex relationship between the fast X-ray variability and the physics of the accretion disk wind, i.e. its origin, dynamics, ionization, structure, and short-timescale evolution. This includes determining whether or not the structure of the wind is constant in time. One could easily imagine a scenario in which the wind is unaffected by the limit cycles in the inner disk, e.g. if it is launched from the outer disk by simple X-ray heating from the phase-averaged X-ray luminosity or by MHD processes (see, e.g. Miller et al. 2006a, 2008). Or perhaps there is a simple relationship between the wind and the variability, where the wind forms independently but, as it rises off the disk, is photoionized by the strong quasi-periodic X-ray variability.

In this section, we exploit the simultaneous strong variability in the accretion disk wind (Figure 12) and the X-ray continuum to argue that neither of these scenarios provides a satisfactory description of the accretion disk wind physics in GRS 1915+105. We use photoionization arguments to probe the accretion dynamics and plasma conditions in the outer disk, and conclude that there must be a powerful coupling between the formation of accretion disk wind and the X-ray luminosity. We argue that photoionization alone is insufficient to produce the observed variability in the wind.

#### 5.3.1. Plasma Conditions and Ionization Balance

In Section 4.2 we showed that the absorbed fluxes in both FeXXV and FeXXVI vary with  $\phi$ . Given the variability in the X-ray absorber, we treat the disk wind as though it is not (in general) in photoionization equilibrium. However, it is reasonable to assume that the observed maxima in the absorbed fluxes occur when the instantaneous photoionization and recombination rates are momentarily equal. Here, under this assumption, we estimate the gas density in the wind.

Neglecting collisional ionization, this temporary ionization balance can be expressed (Liedahl 1999)

$$\frac{1}{4\pi R^2} \Phi_i n_i = \alpha_{i+1} n_e n_{i+1}, \quad (5)$$

where  $R$  is the distance to the continuum source,  $n_e$ ,  $n_i$ , and  $n_{i+1}$ , are the electron density and number density of iron in charge states  $i$  and  $i+1$ ,  $\alpha_{i+1}$  is the recombination rate into charge state  $i$  (out of charge state  $i+1$ ), and  $\Phi_i$  is the ionizing spectrum integrated over the photoionization cross-section  $\sigma_i$  for charge state  $i$ :

$$\Phi_i = \int_{\chi_i}^{\infty} \varepsilon^{-1} \sigma_i(\varepsilon) L_\varepsilon d\varepsilon. \quad (6)$$

Here  $L_\varepsilon$  is the monochromatic luminosity and  $\chi_i$  is the ionization threshold. Given a set of ion fractions (or  $n_i$  and  $n_{i+1}$ ), an ionizing continuum, and appropriate recombination rates, the ionization parameter (Tarter et al. 1969)

$$\xi = \frac{L_X}{n_e R^2} \quad (7)$$

is determined by equations (5) and (6).

In general, the ion fractions depend on the ionizing continuum, the ionization parameter, and the overall density (Kallman & Bautista 2001). However, if the absorption lines are unsaturated, we have an additional constraint from the linear part of the curve of growth, which relates the equivalent width of a spectral line to the ionic column density:

$$\frac{W_\lambda}{\lambda} = \frac{\pi e^2}{m_e c^2} N_i \lambda f_{ij}. \quad (8)$$

Here  $W_\lambda$  is the line equivalent width in mÅ,  $\lambda$  is the wavelength,  $m_e$  is the electron mass,  $c$  is the speed of light,  $N_i$  is the column density of charge state  $i$ , and  $f_{ij}$  is the oscillator strength of the relevant transition.

At  $\phi = 0.54$ , the Fe XXVI line is almost certainly unsaturated because it continues to increase in both absorbed flux and equivalent width for another 20 seconds (for saturated lines, the flux and equivalent width grow very slowly until the optical depth is  $\gtrsim 1000$ ). For this reason, it seems likely that the Fe XXV line is also unsaturated. Using our measured equivalent widths and oscillator strengths from the XSTAR (Kallman & Bautista 2001; Bautista & Kallman 2001) database, we evaluate equation 8 for Fe XXV and Fe XXVI. We find that  $n_{\text{XXVI}}/n_{\text{XXV}} \approx N_{\text{XXVI}}/N_{\text{XXV}} = 2.5$  at  $\phi = 0.54$ .

To recap, under the reasonable assumptions that the wind is optically thin and in temporary ionization equilibrium, we can estimate the density by specifying the location of the wind ( $n_e \propto R^{-2}$ ). Based on the dynamical estimates of Paper I, we set  $R_{\text{wind}} \sim 2.5 \times 10^{11}$  cm. We use photoionization cross-sections from Verner et al. (1996) and recombination rates from XSTAR (T. Kallman, private communication). For temperatures  $10^5 \text{ K} \leq T \leq 10^7 \text{ K}$ , we find that the implied electron density in units of  $\text{cm}^{-3}$  is  $10.8 < \log(n_e) < 12.4$ . For the measured luminosities we can expect the ionization parameter to be between  $10^3$  and  $10^5$ . This is reasonable for a plasma dominated by hydrogen- and helium-like iron.

### 5.3.2. Ionization Parameter and Plasma Dynamics

At the beginning of Section 5.3, we posed the question: is it possible that the structure of the wind is constant in time, so that the variability in the spectral lines is purely due to the changing ionizing luminosity? Here we show that the answer is a resounding ‘no’. This implies that the wind must be re-formed or re-launched each and every cycle. Even without the photoionization considerations that follow, this answer could be anticipated from Figure 12, where it can be seen that between  $\phi = 0.2$  and  $\phi = 0.54$ , the flux in the Fe XXVI and Fe XXV lines are roughly equal, while the X-ray luminosity increases by  $\sim 40\%$  over the same phase interval. It is quite unlikely that these observed line fluxes could be produced purely by photoionization, because the ion fractions for H- and He-like species are only comparable over narrow intervals in  $\xi$  (Kallman & Bautista 2001).

That said, we performed a brief photoionization analysis with XSTAR, using the analytic model WARMABS. Since we are essentially modeling only H- and He-like iron, it should be understood that these models are designed not to give an exhaustive account of the photoionization state of the gas but to parametrize the relationship between the X-ray continuum and the wind. We use

our models of the ionizing spectrum (Section 4.1) at  $\phi = 0.54$  and  $\phi = 0.92$  to generate atomic level populations. We then fit our 6–7.5 keV HETGS spectra for the equivalent hydrogen column density, ionization parameter, and velocity shift of the wind at those phases. We fix the turbulent line width at  $200 \text{ km s}^{-1}$  (Section 4.2; see also Ueda et al. 2009). We set the density at  $n = 10^{12} \text{ cm}^{-3}$ . Our best fits indicate that at  $\phi = 0.54$ , when Fe XXV is maximized, the equivalent hydrogen column density, ionization parameter, and velocity of the accretion disk wind are  $N_{\text{H}} = 2.1_{-0.8}^{+0.7} \times 10^{22} \text{ cm}^{-2}$ ,  $\log \xi = 3.87_{-0.02}^{+0.09}$  ergs  $\text{cm s}^{-1}$ , and  $v = -550_{-390}^{+200} \text{ km s}^{-1}$ . The errors are  $1\sigma$ . At  $\phi = 0.92$ , the maximum of Fe XXVI, we find  $N_{\text{H}} = 10_{-2}^{+6} \times 10^{22} \text{ cm}^{-2}$ ,  $\log \xi = 4.8 \pm 0.1$  ergs  $\text{cm s}^{-1}$ , and  $v = -1520_{-240}^{+230} \text{ km s}^{-1}$  for this disk wind. More detailed analysis would be necessary to account for additional dynamical components at this phase (Fig. 11).

We have already pointed out the changing velocity of the absorber, but we notice here a significant increase in the column density and ionization parameter of the wind (factors of roughly 5 and 7, respectively). During this same phase interval ( $\phi = 0.54 - 0.92$ ) the ionization parameter increases far more than the X-ray luminosity. The luminosity increases by a factor of 2, and the ionizing flux for H- and He-like iron only increases by a factor  $\sim 1.4 - 1.5$ . This is an indication that the luminosity variations are insufficient to produce the observed absorption line variability. The apparent changes in the fitted column density are further evidence that the structure of the wind cannot be constant in time. This, too, could be anticipated from Figure 11, where both the wind ionization state and the strength of the Fe XXVI line change significantly with  $\phi$ .

Admittedly, the exact value of the column density could be underestimated if resonance scattering or thermal emission lines fill in some of the absorption features during the heartbeat cycle (see, e.g. Wojdowski et al. 2003; Kallman et al. 2009). Additionally, the column of Fe XXVI may be enhanced by recombination in the totally ionized wind. However, even if these effects are important, significant ionization evolution in the disk wind is still implied by the fact that Fe XXV disappears while Fe XXVI remains. The appearance of a blue wing in the Fe XXVI line profile near  $\phi = 0.92$  (Figure 11) is a final indication that the structure of the outflow varies substantially during the cycle, probably due to the injection of additional material.

### 5.3.3. Wind Formation Scenarios

The observed strong variability in the accretion disk wind leads to two intriguing conclusions. First, the density and structure of the wind must change on very short timescales. This must be the case because the wind becomes progressively more ionized as the cycle proceeds, but the X-ray luminosity does not increase enough to produce the resulting ionization. Similarly, the distance between the wind and the X-ray source cannot change much in the requisite  $\sim 20$  seconds because the outflow is too slow. Thus equation (7) dictates that the density or structure of the wind must change. Second, these changes in the wind must be quasi-periodic (as observed). Fast quasi-periodic variability in the wind is rather unusual, so we address it first. There are three basic meth-

ods by which the wind might show coherent variability during the cycle:

1. Its structure is constant in time, but its ionization parameter changes in accordance with  $L_X$ .
2. The wind is periodically launched from within or close to the oscillating region of the inner disk.
3. The wind is periodically launched from the outer disk (where previous studies have suggested it originates) by radiation from the inner disk.

Based on simple ionization arguments, we have already ruled out Case 1. Cases 2 and 3 are more complex scenarios, and we weigh their pros and cons in what follows. We are unable to rigorously rule out these scenarios, but the outer-disk origin seems preferable (see below).

For Case 2, let us suppose the wind originates at  $50 R_g$ . Since the phase variations in this region are strong, an oscillating wind seems natural. However, given our measured ionization parameters, the density in the wind would have to be  $n_e \sim 3 \times (10^{17} - 10^{19}) \text{ cm}^{-3}$ . Neither thermal nor radiation-driven winds can produce such dense, highly ionized outflows at such small radii (see Proga & Kallman (2002) and references therein), which would leave MHD processes (Proga 2000; Miller et al. 2006a, 2008). But even if the magnetic field does vary coherently during the  $\rho$  cycle, it is difficult to understand how a wind at  $50 R_g$  could have a velocity as low as  $500 \text{ km s}^{-1}$  and a line width  $\lesssim 800 \text{ km s}^{-1}$ , given that the orbital velocity at  $50 R_g$  is approximately  $40,000 \text{ km s}^{-1}$  for a  $14 M_\odot$  black hole with a spin parameter  $a_* = 0.98$  (McClintock et al. 2006). It is also unclear how this wind could persist for 30 ks given the short infall time at  $50 R_g$ .

For Case 3, let us suppose that the wind originates at  $10 \text{ lt-s}$  from the black hole. At this radius, dynamical and viscous timescales are much too long to produce coherent phase variability. However, the strong continuum variability provides a straightforward origin for the wind: as the bright X-ray burst propagates outwards, it should irradiate the disk in ever-larger annuli, launching a thermally driven wind from each radius. This imprints a strong phase dependence on the wind. In other words, the outer disk and inner disk are linked by radiation.

The most significant challenge for this scenario involves getting the wind into the line of sight quickly, since the inclination of the disk (i.e. the jet axis) is  $66^\circ$ . There are several options to resolve this dilemma, all of which amount to reducing the angle between the plane of the outer disk and the line of sight: (a) Irradiated disks are known to flare vertically at large radii, with scale heights  $H/R \lesssim 0.1$ ; (b) radiation- or tidally-driven warps may be present in the outer disk of GRS 1915+105 (Pringle 1996; Whitehurst & King 1991); (c) the inner disk and outer disk may be misaligned, as suggested by Lee et al. (2002) to connect the overabundance of iron along the line of sight to the geometry of the supernova that formed the black hole (e.g. Brown et al. 2000). With a combination of these possibilities, it may be possible to produce the observed 30–40 second rise time for the wind. However, it should be noted that this scenario, while favored, cannot be fully tested at this time because our HETGS phase resolution is limited. We find that shifting our

$\phi = 0$  times by some constant offset (on top of the random scatter reported in Section 3.2) merely introduces a phase offset into Figure 12. Longer observations of this wind may be able to measure the travel time directly.

Case 3 also has the attractive potential to explain qualitatively a number of the observed properties of the disk wind, especially its increasing column density, ionization parameter, and velocity. The column density increase is simple: more material is launched into the light of sight as time passes. In a thermally-driven wind, the velocity and ionization parameter are proportional to  $R^\gamma$ , and the density decreases like  $n \propto R^{-2-\gamma}$  (Begelman, McKee, & Shields 1983).  $\gamma$  is a power-law index between 0 and 0.5 under equilibrium conditions. If such scaling laws are applicable in our observation, then the increase in  $v$  and  $\xi$  may be partly related to thermal driving of the wind. A robust estimate of  $\gamma$  would require us to determine the precise launch time of the wind, or the point at which the optical depth in the newly-launched wind dominates that of the very highly-ionized wind from the previous cycle. Such a probe is beyond the capabilities of our present data. Simulations of the oscillation-driven wind (Proga et al., in preparation) may shed additional light on these issues.

#### 5.3.4. The Role of the Wind in GRS 1915+105

Finally, we attempt to estimate the mass-loss rate in the wind in our observation. This is particularly important because recent hydrodynamic simulations of thermally-driven winds (Luketic et al. 2010) have shown that such winds can have mass loss rates well above the accretion rate and thus may exert a strong influence on the accretion dynamics of the system. Conditions here are likely to be far from steady state, so we use an elementary consideration based on the maximum column density in the wind. In the cylindrical approximation, which is appropriate if the wind is launched  $\sim$ vertically off the disk,  $\dot{M}_{\text{wind}}$  should scale approximately as

$$\begin{aligned} \dot{M}_{\text{wind}} &= A m N_{\text{H}} / \Delta t_{\text{launch}} & (9) \\ &= 4\pi R_{\text{wind}} v_z m N_{\text{H}}, & (10) \end{aligned}$$

where  $\Delta t_{\text{launch}}$  is the time over which the wind is launched,  $v_z$  is the wind speed perpendicular to the plane of the disk,  $A = 2 \times 2\pi R_{\text{wind}} v_z \Delta t_{\text{launch}}$  is the outer surface area of the cylinder filled by the wind, and  $m$  is the average ion mass per hydrogen atom ( $\sim 2.4 \times 10^{-24} \text{ g}$  assuming ISM abundances from Wilms et al. 2000).

If  $v_z \approx v \approx 1000 \text{ km s}^{-1}$  and  $R_{\text{wind}} = 46 \text{ lt-s}$ , then the implied wind mass loss rate is  $\dot{M}_{\text{wind}} \lesssim 3.9 \times 10^{20} \text{ g s}^{-1}$ , which is roughly 25 times our measured maximum mass accretion rate. In Paper I, we estimated  $\dot{M}_{\text{wind}}$  based on spherical symmetry arguments and the ionization parameter. Our estimate here is consistent with Paper I if the covering factor in the spherical approximation is of order unity. This may be more appropriate for the heartbeat state than for the other *Chandra* observations, since our average HETGS  $\rho$ -state spectrum features a P-Cygni profile with roughly equal emission and absorption components. The kinetic luminosity in the wind is  $\dot{L}_{\text{wind}} \lesssim 10^{36} \text{ ergs s}^{-1}$ , which is far less than the radiative luminosity. Still, if the wind is as massive as implied by our estimates from equation (10), we should



expect it to exert a significant influence on the accretion dynamics in GRS 1915+105.

Shields et al. (1986) argued that very massive thermal winds can excite long-period oscillations in the accretion disk as long as the mass loss rate in the wind is sufficiently high ( $\dot{M}_{\text{wind}} \gtrsim 15\dot{M}$ ) and increases with the accretion rate. As the accretion rate rises, the wind becomes more massive and begins to drain the disk. This emptying quenches the wind, allowing the disk to refill, producing a repetitive cycle. Our  $\dot{M}_{\text{wind}}$  is potentially high enough to produce this long instability, with a period

$$P \approx 3400s \alpha^{-7/9} M^{14/9} T_{\text{IC8}}^{-4/3} \dot{M}_{17}^{-1/3}, \quad (11)$$

where  $M$  is the black hole mass in units of  $M_{\odot}$ ,  $T_{\text{IC8}}$  is the Compton temperature in units of  $10^8$  K, and  $\dot{M}_{17}$  is the mass accretion rate in units of  $10^{17} \text{ g s}^{-1}$ .

Previously, X-ray (Wilms et al. 2001) and optical (Brocksopp, Groot, & Wilms 2001) observations provided strong evidence that this instability may drive soft/hard state transitions in the black hole binary LMC X-3, although no wind was observed directly (Cui et al. 2002; Page et al. 2003). In GRS 1915+105, thermal winds have been suggested as dynamically important (Lee et al. 2002; Rau, Greiner, & McCollough 2003), but only recently has the contribution of this particular massive wind to X-ray variability been measured (Nielsen & Lee 2009; Luketic et al. 2010). For our measured parameters in the heartbeat state of GRS 1915+105,  $P \sim 1.5 \times 10^6$  s, or about 17 days, if  $T_{\text{IC8}} = 1$ . To compare this result to the available data on the  $\rho$  oscillation, we locate all observations of heartbeats in the entire *RXTE* PCA archival lightcurve of GRS 1915+105. Around each pointing, we search for nearby  $\rho$  states in windows of various durations. Statistically, we find that 90% of the pointed observations in a window of width  $12 \pm 5$  days surrounding a  $\rho$  state observation also show heartbeats. We conclude that the period of the Shields oscillation  $P$  is comparable to the typical occupation time for the  $\rho$  state, so that the wind-driven instability may actually be responsible for transitions into/out of this state.

Our results therefore indicate that the accretion disk wind in GRS 1915+105 may play an integral role in transitions between variability classes, effectively acting as a gatekeeper or a valve for the external accretion rate, and facilitating or inhibiting state transitions. In this context, it is notable that all published observations of GRS 1915+105 in a remotely soft or variable state with enough sensitivity to detect highly ionized absorption lines have done so (Kotani et al. 2000; Lee et al. 2002; Ueda et al. 2009; Nielsen & Lee 2009; Ueda et al. 2010). We note that Lee et al. (2002) actually detected these lines in a relatively soft instance of the hard  $\chi$  state, and that we showed in Paper I how the wind is sensitive to the fractional hard X-ray flux, not the specific state.

Although the duration of our observation is clearly too short to probe long-term changes in the accretion flow, it provides us with a useful diagnostic of the slower changes in the disk wind. Inspection of a series of time-resolved spectra (subsets of our observation 3–10 ks in duration) indicates that the average ionization level of the wind may decrease over the course of the 30 ks *Chandra* observation (not unlike the changes detected by Lee et al.

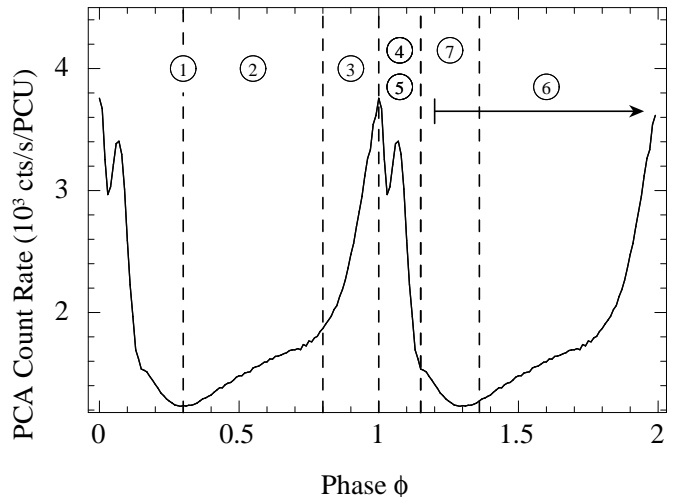


FIG. 14.— The PCA count rate lightcurve for the heartbeat state, labeled to correspond to our physical description of the  $\rho$  cycle in Section 6.

2002; Schulz & Brandt 2002; Ueda et al. 2009). The origin of this change is unclear, and it may have no immediate impact on state transitions: PCA pointed observations show the source to be in the heartbeat state on 2001 May 23 (our observation) and May 30, but not May 16 or June 5. The sampling is hardly sufficient to determine the time of state transitions, but the ASM lightcurves suggest that this  $\rho$  state may have persisted for at least 3–5 days before and after the time interval presented here.

## 6. TRACKING THE CYCLE PHYSICS

For clarity, we present a brief step-by-step summary of our model for the physics of the heartbeat state, beginning at the minimum of the cycle for ease of narration. Each step of this narrative is marked on the X-ray lightcurve in Figure 14. Furthermore, each event is included in Table 3 along with its relevant phase interval, location in the text, and observational evidence. The precise details apply specifically to this observation, but in the future, it may be possible to generalize to other instances of this oscillation.

1. ( $\phi \sim 0.3$ ) A wave of excess material, supplied by the high external accretion rate, originates near  $25R_g$  and propagates radially (inwards and outwards). For  $R \lesssim 100 R_g$ , the disk is always dominated by radiation pressure.
2. ( $\phi = 0.3 - 0.8$ ) Possibly as a result of local Eddington effects, the disk responds by increasing its inner radius (the slow rise) at  $\sim$ constant temperature.
3. ( $\phi = 0.8 - 1.0$ ) During the soft pulse, the disk luminosity increases rapidly. When it reaches its maximum,  $R_{\text{in}}$  drops sharply, possibly at a constant accretion rate. This suggests a disk instability at the end of the density wave. Incidentally, the maximum disk luminosity in this interval is  $\sim 90\%$  of the global Eddington limit for spherical accretion.
4. ( $\phi = 0.0 - 0.1$ ) The instability leads to the ejection of the material from the inner disk, possibly the hot surface layer, which may produce a flash of

TABLE 3  
PHYSICS OF THE  $\rho$  CYCLE

Cycle Event	Phase Interval	§6 Physics	Location ( $R/R_g$ )	Discussed in §x	Observational Evidence
Minimum	$\sim 0.3$	1: Density wave originates, propagates in the inner disk	25	5.1.2	Strong cyclic variations in $L_{\text{disk}}$ and accretion rate; High $L_{\text{disk}}/L_{\text{Edd}}$
Slow Rise	0.3–0.8	2: Local Eddington evolution	1–5	5.1.1–5.1.2	$L_{\text{disk}}$ , $R_{\text{in}}$ , and $\dot{M}$ grow slowly at roughly constant $T_{\text{obs}}$
Soft Pulse	0.8–1.0	3: Disk luminosity rises	1–5	4.1.3, 5.1.2	$\max(L_{\text{disk}}) \lesssim L_{\text{Edd}}^{\text{a}}$
	0.9–1.0	3: Disk becomes unstable, possibly due to radiation pressure	1–5	4.1.3, 5.1.1–5.1.2	Unstable: $R_{\text{in}}$ drops, $T_{\text{obs}}$ spikes; Radiation Pressure: $L_{\text{disk}} \lesssim L_{\text{Edd}}^{\text{a}}$ at constant high $\dot{M}$ ( $L \propto \dot{M}^4/3$ )
Hard Pulse	0.0–0.1	4: Disk ejects material, which collides with corona	1–5	4.1.3, 5.1.3	$E_{\text{fold}}$ , $kT_e$ plummet; Bremsstrahlung normalization spikes
	0.05–0.15	5: Density wave subsides, disk relaxes	1–5	4.1.4, 5.1.1, 5.1.2	$L_{\text{disk}}$ and $T_{\text{obs}}$ drop, $R_{\text{in}}$ grows at constant low $\dot{M}$ ( $L \propto \dot{M}^4/3$ )
Wind Formation	0.2–1.1	6: Intense X-ray heating launches, ionizes a wind from the outer disk	$10^5 - 10^6$	5.3	Fe XXV, Fe XXVI absorption lines grow and then fade; Line widths and blueshifts are non-relativistic
Hard X-ray Tail	0.15–0.36	7: Production of a short-lived jet	$1 - 10^3$	3.3, 4.1.1, 5.1.3	Band-limited noise, high $rms$ ; hard X-ray spectrum; low luminosity

NOTE. — Physical processes in the  $\rho$  cycle are arranged here by phase and by location in the accretion disk, along with observational evidence and relevant sections of the text. Quoted phase intervals are approximate.

<sup>a</sup> Here  $L_{\text{Edd}}$  is the global Eddington limit, i.e. the Eddington limit for spherical accretion.

bremsstrahlung as it collides with the hot corona (the hard pulse).

5. ( $\phi = 0.05 - 0.15$ ) The wave of material subsides; the disk radius moves out quickly at the new (low) accretion rate.
6. ( $\phi = 0.2 - 1.1$ ) The bright X-ray pulses travel out along the disk, providing an impulse of X-ray heating and producing a hot, massive wind, which is subsequently over-ionized. Radiation thus links the dynamics of the inner and outer accretion disks from  $R = 1 - 10^6 R_g$ .
7. ( $\phi = 0.15 - 0.36$ ) The hard X-ray spectrum, high  $rms$ , and band-limited noise near hard X-ray tail and the minimum of the cycle signal the possible production of a short-lived jet. Conditions in the accretion disk and corona are similar to other hard-state-like dips in GRS 1915+105.

## 7. CONCLUSIONS

In this paper, we have presented a detailed analysis of the spectral and timing variability of GRS 1915+105 in the ‘heartbeat’ ( $\rho$ ) state, a 50-second quasi-regular oscillation that usually consists of single- or double-peaked bursts approaching the Eddington luminosity (TCS97, B00). The accretion dynamics in this state are particularly interesting because we find strong periodic variations in both the X-ray continuum and in the accretion disk wind. Our results constitute the very first observational probe of accretion disk wind physics on single-second timescales, nearly four orders of magnitude shorter than the dynamical time at the location of the wind. By performing our analysis with respect to cycle phase (as opposed to time), we gain special insight into the physics that drives the oscillation (the radiation pressure instability and the local Eddington limit) and the origin of the accretion disk wind (transient X-ray heating). We argue that our observation constitutes

a snapshot of an evolutionary process around this black hole, in which the wind and its variability play an integral role in the changing state of the accretion disk on timescales from seconds to weeks or months.

In the context of previous results, we have been able to answer two pressing questions about X-ray variability in GRS 1915+105:

1. What is the origin of the hard pulse in the lightcurve of the  $\rho$  state? Theoretical models predict single-peaked lightcurves (but see JC05), and yet single-peaked cycles account for only 40% of the observed cycles (Neilsen et al. 2011, in preparation).
2. How does the wind know about the variability in the inner accretion disk? This question is extremely important given our argument in Paper I that the wind functions as the mechanism for jet suppression.

Our models of the X-ray continuum suggest that the hard pulse in the lightcurve is produced by the radiation pressure-driven ejection of material from the inner disk. As the ejected plasma collides with the corona, it either produces a burst of bremsstrahlung or becomes so Compton-thick that it scatters nearly all the light from the inner disk. Simulations (NRM00, JC05) have predicted such ejections, but we believe our result constitutes the first spectral detection of the ejected plasma. This type of analysis may be repeated easily for many other variability classes, allowing future detailed characterizations of accretion/ejection physics by X-ray state.

Of great interest is our ability to diagnose and understand these X-ray states in the context of inflow and outflow physics. It is particularly important to establish a clear link between the variability of the inner accretion disk and the wind, without which a connection between the wind and the jet would seem improbable. In our analysis, we find that the fast variability in the X-ray

luminosity of the inner disk can actually produce significant structural changes in the outer disk, producing a disk wind on the same timescales. Our calculations based on equation (11) provide an estimate of (twice) the typical timescale for jet suppression if the wind actively quenches the jet from the outer disk, but it is clear that both fast and slow variations in the accretion rate cannot be neglected in this process. Future observation of states with significant jet and wind activity, like the  $\beta$  state (Mirabel et al. 1998; Neilsen & Lee 2009; Neilsen et al. 2011, in preparation), will reveal further details about the precise nature of the wind-jet interaction.

Finally, we note that instruments like the High Timing Resolution Spectrometer planned for the *International X-ray Observatory (IXO)* will revolutionize fast variability studies of both emission lines (e.g. Miller & Homan 2005) and accretion disk winds in X-ray binaries. With high signal-to-noise, good spectral resolution, and excellent time resolution, it may be possible to perform QPO-phase-resolved reverberation mapping with disk emission lines and wind absorption lines, not only in GRS 1915+105, but in a large subset of the known Galactic black holes. Furthermore, recent *XMM-Newton* studies of Seyfert galaxies have detected variable absorbers dur-

ing long or quasi-periodic dips (NGC 1365, Risaliti et al. 2009; RE J1034+396, Maitra & Miller 2010). The variations, which have been attributed to the orbital motion of the warm absorber, suggest the exciting possibility of a similar database of variability for supermassive black hole systems. Future high-resolution spectral variability studies with *Chandra* and missions like *IXO* will thus allow us to probe even deeper into fundamental accretion physics on all mass scales.

We thank the referee for comments which improved the quality and clarity of our paper. We thank Claude Canizares, Norbert Schulz, Tim Kallman, and Mike Nowak for helpful discussions of spectral variability, and we thank Guy Pooley for making the radio observations publicly available. J.N. and J.C.L. gratefully acknowledge funding support from *Chandra* grant AR0-11004X, the Harvard University Graduate School of Arts and Sciences, and the Harvard University Faculty of Arts and Sciences; R.A.R. acknowledges partial support from the NASA contract to MIT for support of *RXTE* instruments.

*Facilities:* CXO(HETGS), RXTE(PCA)

## APPENDIX

### MEASURING PEAK TIMES

#### *Motivation and Method*

Our primary concern in measuring the peak times for the  $\rho$  cycle is consistency between *RXTE* and *Chandra*. For *RXTE* analysis alone, the single-peaked spectral hardness ratios may provide a simpler method for measuring peak times. But since *Chandra*'s limited bandpass does not allow optimal hardness ratios, we measure peak times from the X-ray count rate. As discussed in Section 3.1, we use a representative cycle as a template for cross-correlation with the entire lightcurve; the peaks in the resulting cross-correlation correspond to the peaks in the lightcurve. We smooth the cross-correlation with a Gaussian of FWHM 3 seconds (much less than the typical width of a correlation peak) and measure the time of maxima via parabolic interpolation. The resulting maxima are preliminary peak times for the lightcurves. We use them to create the average phase-folded lightcurve, which we then use as a new template for cross-correlation. This process mitigates the possible dependence of our results on our initial choice of template.

#### *PCA versus Chandra*

Given the high effective area of the PCA and the high flux of GRS 1915+105, we are confident in our peak times from *RXTE*. However, because S/N in our grating spectra does not allow us to use only the time intervals where both instruments are on-source, we need to be equally confident in our peak times from *Chandra*. We actually find good quantitative agreement between the *Chandra* and PCA peak times during the overlap interval: the mean difference in peak times is  $\Delta T = -0.98 \pm 0.25$  s (where the error is the  $1\sigma$  sample standard deviation for the 273 peaks detected by both instruments). Qualitatively, this means that the *Chandra* peak times precede the *RXTE* peak times and that the noise introduced into the phase ephemeris by using the *Chandra* peak times, corrected by  $\Delta T$ , is much less than the cycle period ( $0.25$  s  $\ll$  50 s). The fact that  $\Delta T$  is non-zero reflects the different instrumental sensitivities of the HETGS and the PCA, since the 2–6 keV lightcurves (normalized to mean count rate) have an RMS difference of 0.1%. The fact that  $\Delta T \sim 1$  s is a numerical coincidence, since the 2–4.5 keV PCA lightcurve peaks  $1.47 \pm 0.19$  s before the full PCA count rate. Physically, the fact that  $\Delta T$  is negative indicates that during this cycle, the hard flux peaks after the soft flux.

## REFERENCES

- Bautista, M. A. & Kallman, T. R. 2001, *ApJS*, 134, 139  
 Begelman, M. C., McKee, C. F., & Shields, G. A. 1983, *ApJ*, 271, 70  
 Belloni, ed. 2010, *Lecture Notes in Physics*, Berlin Springer Verlag, Vol. 794, The Jet Paradigm  
 Belloni, T., Klein-Wolt, M., Méndez, M., van der Klis, M., & van Paradijs, J. 2000, *A&A*, 355, 271  
 Belloni, T., Méndez, M., King, A. R., van der Klis, M., & van Paradijs, J. 1997a, *ApJ*, 488, L109+  
 —. 1997b, *ApJ*, 479, L145+  
 Blum, J. L., Miller, J. M., Cackett, E., Yamaoka, K., Takahashi, H., Raymond, J., Reynolds, C. S., & Fabian, A. C. 2010, *ApJ*, 713, 1244  
 Blum, J. L., Miller, J. M., Fabian, A. C., Miller, M. C., Homan, J., van der Klis, M., Cackett, E. M., & Reis, R. C. 2009, *ApJ*, 706, 60  
 Brocksopp, C., Groot, P. J., & Wilms, J. 2001, *MNRAS*, 328, 139  
 Brown, G. E., Lee, C., Wijers, R. A. M. J., Lee, H. K., Israelian, G., & Bethe, H. A. 2000, *New Astronomy*, 5, 191

- Canizares, C. R., Davis, J. E., Dewey, D., Flanagan, K. A., Galton, E. B., Huenemoerder, D. P., Ishibashi, K., Markert, T. H., Marshall, H. L., McGuirk, M., Schattenburg, M. L., Schulz, N. S., Smith, H. I., & Wise, M. 2005, *PASP*, 117, 1144
- Castro-Tirado, A. J., Brandt, S., & Lund, N. 1992, *IAU Circ.*, 5590, 2
- Cui, W., Feng, Y. X., Zhang, S. N., Bautz, M. W., Garmire, G. P., & Schulz, N. S. 2002, *ApJ*, 576, 357
- Done, C., Wardziński, G., & Gierliński, M. 2004, *MNRAS*, 349, 393
- Eikenberry, S. S., Matthews, K., Morgan, E. H., Remillard, R. A., & Nelson, R. W. 1998, *ApJ*, 494, L61+
- Fabian, A. C., Rees, M. J., Stella, L., & White, N. E. 1989, *MNRAS*, 238, 729
- Fender, R. 2006, *Jets from X-ray binaries*, ed. Lewin, W. H. G. & van der Klis, M., Cambridge Astrophysics Series, No. 39 (Cambridge, UK: Cambridge University Press), 381–419
- Fender, R. & Belloni, T. 2004, *ARA&A*, 42, 317
- Fender, R. P., Garrington, S. T., McKay, D. J., Muxlow, T. W. B., Pooley, G. G., Spencer, R. E., Stirling, A. M., & Waltman, E. B. 1999, *MNRAS*, 304, 865
- Fender, R. P., Pooley, G. G., Brocksopp, C., & Newell, S. J. 1997, *MNRAS*, 290, L65
- Fukue, J. 2004, *PASJ*, 56, 569
- Greiner, J., Cuby, J. G., & McCaughrean, M. J. 2001, *Nature*, 414, 522
- Hannikainen, D. C., Rodriguez, J., Vilhu, O., Hjalmarsdotter, L., Zdziarski, A. A., Belloni, T., Poutanen, J., Wu, K., Shaw, S. E., Beckmann, V., Hunstead, R. W., Pooley, G. G., Westergaard, N. J., Mirabel, I. F., Hakala, P., Castro-Tirado, A., & Durouchoux, P. 2005, *A&A*, 435, 995
- Heinzeller, D. & Duschl, W. J. 2007, *MNRAS*, 374, 1146
- Houck, J. C. 2002, in *High Resolution X-ray Spectroscopy with XMM-Newton and Chandra*, ed. G. Branduardi-Raymont
- Houck, J. C. & Denicola, L. A. 2000, in *Astronomical Society of the Pacific Conference Series*, Vol. 216, *Astronomical Data Analysis Software and Systems IX*, ed. N. Manset, C. Veillet, & D. Crabtree, 591–+
- Janiuk, A. & Czerny, B. 2005, *MNRAS*, 356, 205
- Janiuk, A., Czerny, B., & Siemiginowska, A. 2000, *ApJ*, 542, L33
- Kallman, T. & Bautista, M. 2001, *ApJS*, 133, 221
- Kallman, T. R., Bautista, M. A., Goriely, S., Mendoza, C., Miller, J. M., Palmeri, P., Quinet, P., & Raymond, J. 2009, *ApJ*, 701, 865
- Klein-Wolt, M., Fender, R. P., Pooley, G. G., Belloni, T., Migliari, S., Morgan, E. H., & van der Klis, M. 2002, *MNRAS*, 331, 745
- Kotani, T., Ebisawa, K., Dotani, T., Inoue, H., Nagase, F., Tanaka, Y., & Ueda, Y. 2000, *ApJ*, 539, 413
- Lee, J. C., Reynolds, C. S., Remillard, R., Schulz, N. S., Blackman, E. G., & Fabian, A. C. 2002, *ApJ*, 567, 1102
- Liedahl, D. A. 1999, in *Lecture Notes in Physics*, Berlin Springer Verlag, Vol. 520, *X-Ray Spectroscopy in Astrophysics*, ed. J. van Paradijs & J. A. M. Bleeker, 189–+
- Lightman, A. P. & Eardley, D. M. 1974, *ApJ*, 187, L1+
- Lin, D., Remillard, R. A., & Homan, J. 2009, *ApJ*, 696, 1257
- Luketic, S., Proga, D., Kallman, T. R., Raymond, J. C., & Miller, J. M. 2010, *ApJ*, 719, 515
- Maitra, D. & Miller, J. M. 2010, *ApJ*, 718, 551
- Markwardt, C. B., Swank, J. H., & Taam, R. E. 1999, *ApJ*, 513, L37
- Martocchia, A., Matt, G., Karas, V., Belloni, T., & Feroci, M. 2002, *A&A*, 387, 215
- Massaro, E., Ventura, G., Massa, F., Feroci, M., Mineo, T., Cusumano, G., Casella, P., & Belloni, T. 2010, *A&A*, 513, A21+
- Matt, G., Fabian, A. C., & Ross, R. R. 1993, *MNRAS*, 262, 179
- McClintock, J. E., Shafee, R., Narayan, R., Remillard, R. A., Davis, S. W., & Li, L. 2006, *ApJ*, 652, 518
- Migliari, S. & Belloni, T. 2003, *A&A*, 404, 283
- Mikles, V. J., Eikenberry, S. S., & Rothstein, D. M. 2006, *ApJ*, 637, 978
- Miller, J. M. & Homan, J. 2005, *ApJ*, 618, L107
- Miller, J. M., Raymond, J., Fabian, A., Steeghs, D., Homan, J., Reynolds, C., van der Klis, M., & Wijnands, R. 2006a, *Nature*, 441, 953
- Miller, J. M., Raymond, J., Fabian, A. C., Homan, J., Nowak, M. A., Wijnands, R., van der Klis, M., Belloni, T., Tomsick, J. A., Smith, D. M., Charles, P. A., & Lewin, W. H. G. 2004, *ApJ*, 601, 450
- Miller, J. M., Raymond, J., Homan, J., Fabian, A. C., Steeghs, D., Wijnands, R., Rupen, M., Charles, P., van der Klis, M., & Lewin, W. H. G. 2006b, *ApJ*, 646, 394
- Miller, J. M., Raymond, J., Reynolds, C. S., Fabian, A. C., Kallman, T. R., & Homan, J. 2008, *ApJ*, 680, 1359
- Mirabel, I. F., Dhawan, V., Chaty, S., Rodriguez, L. F., Marti, J., Robinson, C. R., Swank, J., & Geballe, T. 1998, *A&A*, 330, L9
- Mirabel, I. F. & Rodríguez, L. F. 1999, *ARA&A*, 37, 409
- Morgan, E. H., Remillard, R. A., & Greiner, J. 1997, *ApJ*, 482, 993
- Muno, M. P., Remillard, R. A., Morgan, E. H., Waltman, E. B., Dhawan, V., Hjellming, R. M., & Pooley, G. 2001, *ApJ*, 556, 515
- Nayakshin, S., Rappaport, S., & Melia, F. 2000, *ApJ*, 535, 798
- Neilsen, J. & Lee, J. C. 2009, *Nature*, 458, 481
- Page, M. J., Soria, R., Wu, K., Mason, K. O., Cordova, F. A., & Priedhorsky, W. C. 2003, *MNRAS*, 345, 639
- Paul, B., Agrawal, P. C., Rao, A. R., Vahia, M. N., Yadav, J. S., Seetha, S., & Kasturirangan, K. 1998, *ApJ*, 492, L63+
- Pooley, G. G. & Fender, R. P. 1997, *MNRAS*, 292, 925
- Pringle, J. E. 1996, *MNRAS*, 281, 357
- Proga, D. 2000, *ApJ*, 538, 684
- Proga, D. & Kallman, T. R. 2002, *ApJ*, 565, 455
- Rau, A., Greiner, J., & McCollough, M. L. 2003, *ApJ*, 590, L37
- Remillard, R. A. & McClintock, J. E. 2006, *ARA&A*, 44, 49
- Reynolds, C. S. & Nowak, M. A. 2003, *Phys. Rep.*, 377, 389
- Reynolds, M. T. & Miller, J. M. 2010, *ApJ*, 723, 1799
- Risaliti, G., Miniutti, G., Elvis, M., Fabbiano, G., Salvati, M., Baldi, A., Braito, V., Bianchi, S., Matt, G., Reeves, J., Soria, R., & Zezas, A. 2009, *ApJ*, 696, 160
- Schulz, N. S. & Brandt, W. N. 2002, *ApJ*, 572, 971
- Shields, G. A., McKee, C. F., Lin, D. N. C., & Begelman, M. C. 1986, *ApJ*, 306, 90
- Soleri, P., Belloni, T., & Casella, P. 2008, *MNRAS*, 383, 1089
- Steiner, J. F., McClintock, J. E., Remillard, R. A., Narayan, R., & Gou, L. 2009, *ApJ*, 701, L83
- Taam, R. E., Chen, X., & Swank, J. H. 1997, *ApJ*, 485, L83+
- Tagger, M., Varnière, P., Rodriguez, J., & Pellat, R. 2004, *ApJ*, 607, 410
- Tarter, C. B., Tucker, W. H., & Salpeter, E. E. 1969, *ApJ*, 156, 943
- Ueda, Y., Honda, K., Takahashi, H., Done, C., Shirai, H., Fukazawa, Y., Yamaoka, K., Naik, S., Awaki, H., Ebisawa, K., Rodriguez, J., & Chaty, S. 2010, *ApJ*, 713, 257
- Ueda, Y., Yamaoka, K., & Remillard, R. 2009, *ApJ*, 695, 888
- Verner, D. A., Ferland, G. J., Korista, K. T., & Yakovlev, D. G. 1996, *ApJ*, 465, 487
- Vilhu, O. & Nevalainen, J. 1998, *ApJ*, 508, L85
- Whitehurst, R. & King, A. 1991, *MNRAS*, 249, 25
- Wilms, J., Allen, A., & McCray, R. 2000, *ApJ*, 542, 914
- Wilms, J., Nowak, M. A., Pottschmidt, K., Heindl, W. A., Dove, J. B., & Begelman, M. C. 2001, *MNRAS*, 320, 327
- Wojdowski, P. S., Liedahl, D. A., Sako, M., Kahn, S. M., & Paerels, F. 2003, *ApJ*, 582, 959
- Zdziarski, A. A., Johnson, W. N., & Magdziarz, P. 1996, *MNRAS*, 283, 193
- Zimmerman, E. R., Narayan, R., McClintock, J. E., & Miller, J. M. 2005, *ApJ*, 618, 832
- Życki, P. T., Done, C., & Smith, D. A. 1999, *MNRAS*, 309, 561